Published in final edited form as:
Adv Funct Mater. 2023 January 10; 33(2): . doi:10.1002/adfm.202209971.

A Dual-network Nerve Adhesive with Enhanced Adhesion Strength Promotes Transected Peripheral Nerve Repair

Wen Xue,
Department of Internal Medicine, Mary & Dick Holland Regenerative Medicine Program, University of Nebraska Medical Center, Omaha, Nebraska 68198, USA.

Wen Shi,
Department of Internal Medicine, Mary & Dick Holland Regenerative Medicine Program, University of Nebraska Medical Center, Omaha, Nebraska 68198, USA.

Mitchell Kuss,
Department of Internal Medicine, Mary & Dick Holland Regenerative Medicine Program, University of Nebraska Medical Center, Omaha, Nebraska 68198, USA.

Yunfan Kong,
Department of Internal Medicine, Mary & Dick Holland Regenerative Medicine Program, University of Nebraska Medical Center, Omaha, Nebraska 68198, USA.

Olawale A Alimi,
Department of Internal Medicine, Mary & Dick Holland Regenerative Medicine Program, University of Nebraska Medical Center, Omaha, Nebraska 68198, USA.

Hanjun Wang,
Department of Anesthesiology, University of Nebraska Medical Center, Omaha, Nebraska 68198, USA.

Dominick J DiMaio,
Department of Pathology and Microbiology, University of Nebraska Medical Center, Omaha, Nebraska 68198, USA.

Cunjiang Yu,
Department of Biomedical Engineering, Pennsylvania State University, University Park, Pennsylvania 16802, USA.

Bin Duan

---

bin.duan@unmc.edu .

Author contributions: W.X., W.S., and B.D. conceived the study idea. W.X. and B.D. designed the experiments. W.X., W.S., M.K., Y.K., O.A., and H.W. performed the experiments and analysis. All authors contributed to writing the manuscript, discussing the results and implications and editing the manuscript at all stages. The authors acknowledge Wendy A. Schwendeman from Comparative Medicine of UNMC for the rat peripheral nerve anastomosis surgery; Dr. Bing Xue from the Tissue Sciences Facility of UNMC for the paraffin section of peripheral nerves; and Nicholas H. Conoan from Electron Microscopy Core Facility for the TEM imaging.

Competing interests: The authors declare that they have no competing interests.

Supporting Information
All relevant data are included in the main manuscript and the Supporting Information. Additional data are available from the corresponding author upon reasonable request.

Department of Internal Medicine, Mary & Dick Holland Regenerative Medicine Program, University of Nebraska Medical Center, Omaha, Nebraska 68198, USA.

Department of Surgery, University of Nebraska Medical Center, Omaha, Nebraska 68198, USA.

Department of Mechanical and Materials Engineering, University of Nebraska-Lincoln, Lincoln, Nebraska 68588, USA.

Abstract

Peripheral nerve transection has a high prevalence and results in functional loss of affected limbs. The current clinical treatment using suture anastomosis significantly limits nerve recovery due to severe inflammation, secondary damage, and fibrosis. Fibrin glue, a commercial nerve adhesive as an alternative, avoids secondary damage but suffers from poor adhesion strength. To address their limitations, a highly efficacious nerve adhesive based on dual-crosslinking of dopamine-isothiocyanate modified hyaluronic acid and decellularized nerve matrix is reported in this paper. This dual-network nerve adhesive (DNNA) shows controllable gelation behaviors feasible for surgical applications, robust adhesion strength, and promoted axonal outgrowth *in vitro*. The *in vivo* therapeutic efficacy is tested using a rat-based sciatic nerve transection model. The DNNA decreases fibrosis and accelerates axon/myelin debris clearance at 10 days post-surgery, compared to suture and commercial fibrin glue treatments. At 10 weeks post-surgery, the strong adhesion and bioactivity allow DNNA to significantly decrease intraneural inflammation and fibrosis, enhance axon connection and remyelination, aid motor and sensory function recovery, as well as improve muscle contraction, compared to suture and fibrin treatments. Overall, this dual-network hydrogel with robust adhesion provides a rapid and highly efficacious nerve transection treatment to facilitate nerve repair and neuromuscular function recovery.

Graphical Abstract

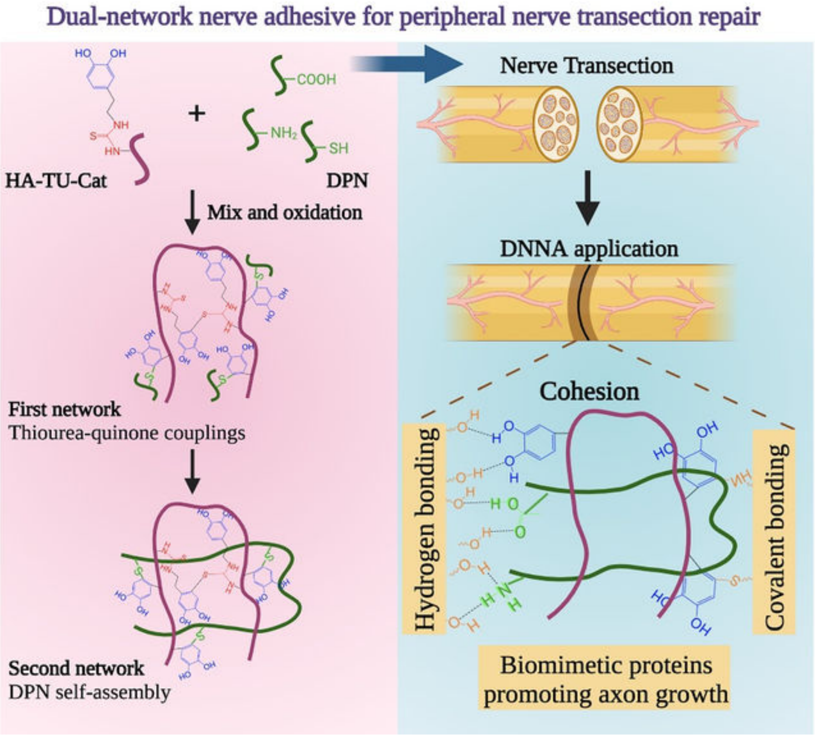

A dual-network nerve adhesive (DNNA) is developed based on dopamine-isothiocyanate modified hyaluronic acid (HA-TU-Cat) and decellularized nerve matrix (DPN). HA-TU-Cat crosslinks quickly through thiourea-quinone couplings to form the first network. DPN is bioactive and self-assembles physically into the second network. The two networks covalently bound with each other, enhancing the adhesion strength and promoting axonal growth.

Keywords

bioadhesive; catechol; decellularized matrix; nerve regeneration

1. Introduction

The peripheral nerve transection, an intractable clinical problem, is usually caused by traumatic injuries or medical conditions.[1] It can significantly affect and lead to the loss of motor activity and sensation in the respective part of the body.[2] The current clinical standard treatment for peripheral nerve transection is to coapt injured nerves end-to-end using sutures.[3] The proximal and distal nerve ends are connected to shorten the axonal reconnection distance through epineural or perineural suturing in a tension-free manner.[4] However, the presence of the foreign suture material leads to intraneural inflammation, increased fibrosis, and scar tissue formation.[4] This further results in misalignment of axons, delayed remyelination, and failed nerve recovery.[5] At present, up to 33% of peripheral nerve injuries in clinics exhibit incomplete nerve recovery and poor functional outcomes, including the loss or partial recovery of motor and sensory function, chronic pain, and end target muscle atrophy and weakness.[6] Besides limited efficacy, the microsurgical suturing procedure is time-consuming[7] and introduces multiple needle passages through the nerve epineurium and perineurium. This secondary damage further induces inflammation and aggravates fibrosis.[4, 8] Nerve adhesives are promising alternatives to sutures since they provide a fast and convenient way to connect injured nerve ends. By avoiding secondary tissue trauma, nerve adhesive treatment can potentially decrease inflammation and fibrosis. Among them, fibrin glues are commercially available, biocompatible, possess the longest application history, and have been used in human and many animal studies with the belief that they will minimize the induced trauma.[9] However, in clinical practice, concerns remain about the lack of adequate adhesion strength for fibrin glue treatment alone, due to its weak physical wrapping around the nerve.[10] A biomechanical study of rabbit sciatic nerve transection repair reported a 4-time inferior load to failure/gapping strength with fibrin glue relative to suture after treatment.[11] Similar inferior load to failure results have been found in a rat sciatic nerve model immediately and 7 days after surgery.[12] Due to its mechanical limitations, in clinical practice, fibrin glue is predominantly used as an adjunct to sutures or to coapt nerves where suturing is not possible, for example, intervertebral foramen.[10] Therefore, there is a critical need for a next-generation nerve adhesive with enhanced adhesion.

Several new designs have been explored to enhance the strength and mechanics of tissue adhesives. Most of them utilize various reactive groups to achieve covalent bonding with tissue surface. The reactive groups typically include N-hydroxysuccinimide (NHS) esters,[13] cyanoacrylates,[14] aldehydes,[15] and catechol.[16] NHS esters react with primary amines in tissues to form amide bonds spontaneously and fast, but its susceptibility to hydrolysis impedes the adhesion stability.[17] Cyanoacrylates, with an alkoxy carbonyl group and a nitrile group in the monomer, achieve strong covalent crosslinking with the tissue during polymerization. However, their clinical use is limited by potential toxicity concerns.[18] Despite their potential for strong bonding with amines and thiols in tissues, the use of aldehydes often raises risks of cytotoxicity.[19] Among them, catechol-based glues, inspired by the strong underwater adhesion of mussels, have generated tremendous research interests in developing tissue adhesives, including nerve adhesives.[20, 21] Catechol (Cat) is the sidechain and adhesive moiety of dihydroxyphenylalanine (DOPA) residue, which is believed to be the key component in adhesive mussel foot proteins.[21–23] After oxidation, the catechol group is converted to quinone, which can self-polymerize through a quinone-quinone complex and bonds with tissues covalently (through nucleophiles, like amines, thiols, and imidazoles).[24] However, this process has its limitations. First, quinone-quinone self-polymerization is random and inefficient, and the curing time ranges from dozens of minutes to hours, which is beyond the surgical time frame.[25] Second, a large amount of quinone is accumulated during this process, undergoing reversible redox cycling.[26] This redox cycling activates reactive oxygen species (ROS), produces reactive semiquinone, increases inflammation, delays axon growth, and is highly cytotoxic.[27] However, nerve adhesives have high requirements on their bioactivity and supportive environment for axonal regrowth, besides the prerequisite of adhesion strength. Therefore, there is still an unmet need for a nerve adhesive that is bioactive, feasible for surgery, and supports the nerve regeneration process.

To address the issues of current nerve glues, we developed a novel catechol-based nerve adhesive, dual-network nerve adhesive (DNNA). Different from conventional catechol-based adhesives, in the DNNA, dopamine-isothiocyanate containing catechol and thiourea (TU) groups was conjugated to hyaluronic acid (HA), a well-known component of the endoneurial extracellular matrix (ECM),[28] to obtain HA-TU-Cat. HA-TU-Cat was then crosslinked with decellularized peripheral nerve matrices (DPN), a promising natural material with bioactive peptides and growth factors. HA-TU-Cat can also self-polymerize through quinone-thiourea couplings. Unlike the quinone-quinone complex, the quinone-thiourea coupling has been reported to be efficient, strong, and reduce quinone back to catechol.[29, 30] All of these allow our DNNA to gelate rapidly, achieve strong adhesion, and decrease quinone accumulation. We therefore hypothesize that this strong and bioactive catechol-based adhesive can reconnect injured nerves and enhance nerve recovery.

Herein, we described the fabrication of DNNA for nerve transection treatment. Its gelation behavior and physical and chemical performance were thoroughly characterized. Robust adhesion strength was determined through lap shear and tensile tests *ex vivo*. The safety and biocompatibility of our adhesive were verified using *in vitro* Schwann cell (SC) proliferation and dorsal root ganglion (DRG) neurite outgrowth. The *in vivo* therapeutic efficacy of DNNA was studied using a rat-based sciatic nerve transection model at 10-day and 10-week post-surgery. Systematic investigations in terms of motor and sensory function recovery, nerve reconnection and remyelination, and muscle structure and function were conducted and compared with the clinical suture treatment and commercial fibrin glues. Importantly, the strong adhesion and bioactivity allowed our adhesive to significantly decrease intraneural inflammation and fibrosis, enhance aligned axon connection and remyelination, aid motor and sensory function recovery, as well as muscle contraction, compared to suture and fibrin treatments. Overall, we propose an innovative and efficacious adhesive hydrogel for the repair and functional recovery of challenging peripheral nerve transections.

2. Results and discussions

2.1 Concept and design of DNNA

Figure 1 shows the concept and design of our catechol-based DNNA. HA is an important endoneurial ECM component, which can reduce scar formation in peripheral nerve injuries,[31] and is chosen as the polymer backbone for catechol-functionalization. It is modified by dopamine-isothiocyanate to obtain Cat and TU groups simultaneously (HA-TU-Cat in Figure 1A). After oxidation, HA-TU-Cat crosslinks quickly through uniform and strong thiourea-quinone couplings, forming the first network (Figure 1B). DPN, a promising nerve-specific biomaterial with abundant bioactive peptides and growth factors, is then incorporated. DPN self-assembles physically into the second network. The two networks covalently interact with each other through quinone in HA-TU-Cat and nucleophiles in DPN, forming the DNNA. When the DNNA is applied to the injured nerve ends, it connects nerve ends through quinone bonding to amines and thiols on the tissue surface covalently or noncovalently through hydrogen bonding (Figure 1C). The two interacted polymer networks in our adhesive serve three important roles: 1) HA-TU-Cat ensures strong hydrogel adhesion and cohesion, feasible curing time for clinical application, and reduced quinone accumulation; 2) DPN provides abundant bioactive proteins, growth factors, and ECM components for axon regrowth; 3) interactions between HA-TU-Cat and DPN further reduce quinone amount and improve hydrogel cohesion, which could help resist failure and crack formation of the bulk matrix and increase adhesion strength, thereby.

2.2 Fabrication and characterization of DNNA

Based on our design concept, we described the detailed fabrication and characterization of our dual-network nerve adhesive here. Catechol-modified HA was prepared in two ways for comparison, namely, the Schiff base condensation and the isothiocyanate–amine coupling. The Schiff base was formed between the aldehyde-modified HA and dopamine, resulting the catechol-modified HA conjugates (HA-Cat), as reported before.[22] Its successful synthesis was confirmed by ^{1}H Nuclear Magnetic Resonance (^{1}H NMR), as indicated by the presence of catechol aromaticproton peaks at $\delta \sim 7$ ppm and catechol methylene-proton peaks at δ 3.1 and 2.8 ppm (Figure S1A). The catechol group grafting ratio in HA-Cat was about 40%. In the second approach, we synthesized the dopamine-isothiocyanate derivative as reported in,[30] which was then grafted onto the HA-adipic dihydrazide (HA-ADH) backbone via isothiocyanate–amine coupling, thereby producing HA-TU-Cat (Figure 1A). The ^{1}H NMR of HA-ADH, dopamine-isothiocyanate, and HA-TU-Cat were shown in Figure S1B–D, respectively. The degree of substitution (DS) of catechol groups in HA-TU-Cat was determined to be about 20%.

Decellularized porcine nerves were prepared based on our previously reported protocols.[32] Hematoxylin and eosin (H&E) staining revealed loosened matrix structures of nerves and absent nuclei after decellularization, as shown in Figure S2A. The deoxyribonucleic acid (DNA) content in porcine native peripheral nerves (NPN) decreased from 514 ± 77 ng/mg to 39 ± 12 ng/mg after decellularization, which met the international requirement of 50 ng/mg (Figure S2B).[33] The collagen and glycosaminoglycan (GAG) concentrations slightly decreased, but no significant differences were detected (Figure S2B). All these results proved successful decellularization and collagen/GAG maintenance of porcine peripheral nerves.

In order to produce in situ curable adhesive hydrogels, oxidation is required to induce crosslinking of catechol-based polymers and to connect tissues covalently. In this study, both a chemical oxidizing agent, i.e., sodium periodate ($NaIO_4$), and an enzymatic oxidizing agent, i.e., mushroom tyrosinase (MT), were implemented. Compared to $NaIO_4$, MT is advantageous due to its high specificity and biocompatibility.[34] 2500 U/mL MT was added to induce HA-Cat (2%) gelation. After being incubated at 37 °C for 24 h, the color of the HA-Cat solution became dark (Figure 2A). However, hydrogel formation was not noticed. We then switched to $NaIO_4$ to accelerate catechol oxidation, and HA-Cat gelated after 30 min of incubation at room temperature with a 1:1 molar ratio of $NaIO_4$ to catechol groups. In contrast, successful gelation of HA-TU-Cat (2%) and DNNA (1% HA-TU-Cat + 1% DPN) was induced after a 500 U/mL MT addition and incubation at 37 °C for 5 min, indicating quick gelation behavior and feasibility for surgical application. Different from dark color of the HA-Cat hydrogel, the HA-TU-Cat and DNNA hydrogels were greyish, suggesting less accumulated quinone groups (Figure 2A). It indicated that quinone-thiourea couplings could reduce quinone amount in the matrix compared to quinone-quinone complex.

To further unveil the role of DPN on quinone consumption in DNNA, ultraviolet-visible (UV-vis) spectroscopy was recorded before and after the addition of MT. As shown in Figure 2B, the quinone peak (~365 nm) appeared 10 min after the addition of MT and became stronger throughout the gelation time in HA-TU-Cat. Since HA-TU-Cat and DNNA gelated with the participation of quinone groups in 5 min (as shown by successful gelation within 5 min in Figure 2A), the catechol group was speculated to turn into quinone after the addition of oxidants but was reduced back to catechol when bonding covalently with TU groups. TU could delay and protect catechol from overoxidation and cytotoxicity from quinone thereby. However, MT oxidized the catechol into quinone continuously, even after the depletion of TU. Thus, the quinone peak became stronger with increasing oxidation time. In regards to the DNNA with a decellularized matrix, an inconspicuous quinone peak appeared 30 min after the addition of MT (Figure 2B) and stayed low even after a 3-hour reaction, compared to HA-TU-Cat (Figure S3). This result indicated that, compared to HA-TU-Cat, the covalent bonding of amines/thiols inside DPN with quinone could further decrease quinone amount, which was favorable for adhesion enhancement and limiting reactive oxygen species.

The modulus of adhesive hydrogel was investigated to determine its cohesion. According to the time sweep rheological analysis (Figure 2C), 2% HA-TU-Cat displayed quicker gelation behavior and higher storage modulus (G”, 45 times) than those of 2% HA-Cat hydrogels, even though the DS of HA-Cat was twice that of HA-TU-Cat. The differences in the gelation and mechanical properties of HA-Cat and HA-TU-Cat were attributed to different gelation mechanisms, where HA-Cat crosslinked through quinone self-polymerization, while HA-TU-Cat crosslinked through quinone-thiourea couplings,[29] which were more uniform and efficient.[35] We also noticed that the addition of DPN into HA-TU-Cat resulted in a significantly higher storage modulus of DNNA (1% HA-TU-Cat + 1% DPN) than that of 1% DPN and 1% HA-TU-Cat individually (Figure 2D). This indicated that the DNNA was more than just a physical mixture of DPN and HA-TU-Cat. Networks formed by DPN and interactions between DPN and HA-TU-Cat networks strengthened the cohesion of DNNA hydrogels.

We also found that the MT concentration did not show significant influence on the G’ of HA-TU-Cat (Figure S4A), but a higher MT concentration did shorten the gelation time (the time when storage modulus was higher than loss modulus) from around 5 min to 1 min when MT concentration increased from 250 U/mL to 2500 U/mL (Figure S4B). 500 U/mL MT was chosen to allow enough operation time as well as potential adjustment during surgery. For future clinical applications, we can further regulate the gelation time through MT concentration according to the surgical needs. But for commercial fibrin glues, they crosslink rapidly (within 1 min), which restricts any further position adjustments once applied. For HA-Cat with different $NaIO_4$ concentrations, as shown in Figure S4C, the 1:0.5 molar ratio of catechol to $NaIO_4$ illustrated similar storage modulus and loss modulus (G”), while the 1:1 ratio demonstrated higher G’ than G”. Thus, the 1:1 ratio was chosen in our further studies.

The morphologies of HA-Cat, HA-TU-Cat, and DNNA were evaluated by scanning electron microscopy (SEM), shown in Figure 2E and Figure S5. All hydrogels showed porous and interconnected structures. The incorporation of DPN seemed to introduce more fiber-like structures into DNNA. The HA-Cat fully dissociated within 14 days *in vitro*, which was faster than HA-TU-Cat and DNNA (Figure 2F). HA-TU-Cat and DNNA illustrated comparable stability, with around 25% mass loss after 14 days. Hydrogel hydrolytic stability normally depends on the cleavage of chemical bonds among polymer backbones. The quinone-quinone oligomerization structure in HA-Cat is random and inefficient. Therefore, it renders the HA-Cat more hydrolytically labile, which leads to a faster dissociation and mass loss of HA-Cat. However, quinone-thiourea couplings in HA-TU-Cat and DNNA are more stable. All hydrogels exhibited gradual swelling over time and reached equilibrium after 20 h (Figure 2G). HA-Cat had a higher swelling ratio than that of HA-TU-Cat and DNNA. The stability and swelling results were consistent with the random oligomerization structure in HA-Cat and the uniform quinone-thiourea couplings in HA-TU-Cat and DNNA.

2.3 Robust adhesion of DNNA

Nerves are subjected to different deformations during daily walking and exercise, including shear and stretch. The adhesive performances of DNNA were evaluated through lap shear and tensile tests to determine its shearing and tensile resistance, respectively, and compared to commercial fibrin glues.

A lap shear test based on fresh porcine skins was applied to assess the ability of adhesives to withstand the stress in a plane when shear forces displaced two skins joined by the adhesive. Figure 3A shows the displacement-force curves of HA-Cat, HA-TU-Cat, DNNA, and commercial fibrin glues. DNNA demonstrated a remarkably increased adhesion force, as well as failure displacement, compared to its counterparts. The adhesion strength was further calculated. DNNA illustrated 5 times higher values compared to fibrin glue and HA-Cat (Figure 3B). In comparison to HA-TU-Cat, the addition of DPN significantly improved the shear resistance ability of the DNNA (Figure 3B). The successful function of adhesives not only depends on the adhesion between adhesives and tissues but also the cohesion among the adhesive matrix.[36] On one hand, DPN introduced more nucleophiles into the DNNA, which increased its hydrogen bonding with tissues. On the other hand, the addition of DPN strengthened the cohesion of DNNA hydrogels. In DNNA, besides quinone-thiourea couplings, DPN self-assembled and neutrophils from DPN could covalently bond with oxidized catechol from HA-TU-Cat. These reactions greatly enhanced DNNA cohesion and adhesion, compared to HA-TU-Cat.

Stretch is another common deformation of nerves, especially for transected nerves undergoing strong retraction due to the elastic endoneurium.[37] A tensile test was used to pull two nerves connected by adhesives to determine stretching adhesion forces. The DNNA showed a higher failure force and adhesion strength than HA-Cat, but no significant difference was observed between HA-TU-Cat and DNNA (Figure 3C and Figure 3D). Although there was weak shear adhesion performance, the tensile force and tensile adhesion strength of fibrin were high and had no statistical differences with those of DNNA (Figure 3C and Figure 3D). We speculated that the enhanced adhesion performance of DNNA was not shown in the tensile tests due to smaller contact area and less hydrogel amount applied (200 μL for the lap shear test and 20 μL for the tensile test), compared to the lap shear test through porcine skins.

To qualitatively show the adhesion performance of the DNNA for peripheral nerve anastomosis, a rabbit sciatic nerve was transected into three sections (Figure 3E-a), and the DNNA was applied at the nerve ends to adhere them (Figure 3E-b). After gelation at 37 °C for 5 min, the reconnected nerve was hung by a pair of tweezers, and the DNNA could successfully bear the reconnected nerve weight. In situ adhesion of a transected rabbit sciatic nerve was also demonstrated after 5 min at room temperature, and the adhesive nerve can even withstand a slight stretch by a blade (Figure 3E-c). DNNA with green food dye was applied onto the surface of porcine skins. The gelated DNNA showed strong adhesion to the porcine skin, as evidenced by the capability to withstand external deformations like twisting, soaking in PBS for 30 min (Figure 3F-a), and flushing under running water for 5 min (Figure 3F-b and Supplementary Video S1). Longer time in PBS was shownIn addition to porcine skins, adherent hydrogels on slides were also able to bear flushing under water (Figure 3F-c and Supplementary Video S2).

Overall, these quantitative results demonstrated stronger adhesion of DNNA compared to fibrin glues. The addition of DPN further significantly improved hydrogel shearing adhesion resistance. The robust adhesion performance of the DNNA in tissues, slides, and wet environments was also confirmed qualitatively.

2.4 DNNA supports SC proliferation and promotes neurite outgrowth *in vitro*

SCs and peripheral axons are two of the most important cell types during peripheral nerve injury and repair processes. SCs are responsible for myelin sheath and axonal debris clearance, providing essential trophic support for injured neurons and further remyelination. Peripheral neuron axonal outgrowth and myelination reflect the nerve injury repair status. The bioactivity and biocompatibility of the decellularized matrix in DNNA were evaluated through SC proliferation and neurite outgrowth *in vitro*.

Primary rat SCs were encapsulated within HA-TU-Cat and DNNA hydrogels, and they were alive in both hydrogels after 7 days (Figure 4A). A spherical cell shape without spreading was also noticed in both hydrogels. SCs proliferated significantly from day 3 to day 7 in both HA-TU-Cat and DNNA, and the addition of DPN did not significantly affect cell growth rate (Figure 4B). The main reason DPN incorporation did not efficiently promote SCs spreading and growth was that hydrogel mechanics regulated cell behaviors besides hydrogel composition. In our previous work, SCs were encapsulated within two concentrations of commercial rat collagen hydrogels (0.15% and 0.4%) and decellularized rat nerve hydrogels (0.4% and 0.9%).[32] We found that SCs in two concentrations of collagen hydrogels had the spherical shape without spreading. For decellularized nerve hydrogels, 0.9% ones with storage moduli around 100 Pa also illustrated spherical cell shape and lower proliferation rate, while cells in 0.4% ones with moduli around 20 Pa illustrated strong SC remodeling capacities, with spreading morphology and higher cell proliferation rates. The results indicated that, apart from the material composition, hydrogel mechanics also played important roles in regulating SC behaviors. In our current study, both DNNA and HA-TU-Cat had storage moduli above 100 Pa, which may lead to weak cell remodeling abilities. Besides, it was reported that despite round morphology of encapsulated SCs in the decellularized matrix *in vitro*, SCs illustrated high viability and maintained functionality after transplantation *in vivo*.[38]

In contrast to SC growth behaviors, the addition of DPN remarkably improved axonal outgrowth from the DRGs (Figure 4C). Tubulin beta III (TUBB3) stained axons had longer extension distances and more branches in the DNNA than those in HA-TU-Cat hydrogels. A semiquantitative measurement illustrated 5 times longer neurite length in the DNNA than those in HA-TU-Cat hydrogels without the decellularized matrix (Figure 4D). Consistent with previous studies, DPN facilitated DRG neurite outgrowth and hydrogel composition was dominant in regulating neurite behaviors, compared to hydrogel mechanics.[32] Bioactive ECM components in the DPN and peptides/growth factors generated after hydrogel degradation were reported to play important roles. For example, it was suggested that collagen IV in DPN could promote neurite attachment and growth through integrin ITGA1.[39] Laminin was also abundantly found in DPN and played positive roles in neurite extension.[32]

The results here verified good biocompatibility of our adhesive and positive role of bioactive components from decellularized nerve matrix, which could facilitate axonal outgrowth and branching.

2.5 DNNA accelerates the axon and myelin debris clearance *in vivo*

To test the therapeutic efficacy of DNNA and compare it with a clinical standard suture and a commercial fibrin glue, we applied them for nerve anastomosis in a rat-based nerve transection model (Figure 5A). After 10 days of surgery, the injured nerves were collected for short-term histological analysis. We performed Masson’s Trichrome (Figure 5B) and H&E (Figure 5C and Figure S6) staining of harvested sciatic nerves. In Figure 5B, collagen-rich fibrotic tissues were found in the suture and fibrin repaired nerves, while there were much less in the DNNA group (indicated by the arrows in Figure 5B). Besides, compared to fibrin and DNNA adhesives, the suture application caused nerve structure interruption and axon mis-direction. Residual sutures and hydrogels without complete degradation were observed in suture and DNNA treated nerves, respectively. According to the H&E staining, foreign body granulomas with abundant nuclei surrounding the residual suture were noted in the suture group (Figure 5C). There were also some foreign body reactions at the boundary between the hydrogel and the nerve in the DNNA group (Figure 5C). For fibrin treated nerve, although no obvious hydrogel residue was detected, many proliferative fibroblasts disrupted nerve fascicle structures (Figure 5C). Moreover, it was worth noting that TUBB3 and myelin basic protein (MBP) staining showed little axon and myelin debris in our DNNA adhesive at the injury site. In contrast, plentiful remaining myelin and axon debris still existed in the suture and fibrin treated nerves (Figure 5D).

During the early stage of nerve injury and repair, macrophages help clear axon and myelin debris to create a microenvironment conducive for axonal regrowth and reconnection, which is an essential part of Wallerian degeneration.[40] But large numbers of macrophages can also lead to intraneural inflammation and fibrosis formation. We thus applied CD68 staining to examine any difference of macrophages in different treatments. As shown in Figure S7, no significant difference was shown in three groups regarding macrophage intensity and number. One possible explanation for different debris clearance results is that similar amounts of macrophages infiltrated but took different responsibilities in different groups. The infiltrated macrophages contributed to fibrosis induction in the suture and fibrin repaired nerves, whereas with the regulation of bioactive decellularized matrix, the macrophages helped with the Wallerian degeneration in the DNNA group. We speculated that those macrophage contribution differences were caused by the treatment methods and hydrogel materials applied. Suture treatment had secondary damage and foreign body reactions, and the fibrin persistence at injury sites was reported to be linked to increased fibrosis.[41] It was demonstrated that the rate of collagen synthesis increased in a three-dimensional fibrin matrix, as opposed to a collagen matrix.[42] In contrast, the incorporated decellularized matrix in the DNNA has been reported to positively regulate the immune responses after nerve injury.[39, 43] It was probable that the body took embedded signaling cues from the DPN and used these cues to direct the *in vivo* remodeling process.

2.6 DNNA promotes nerve sensory and motor function recoveries

Sensory and motor function recoveries are important aspects of nerve regeneration after transection. Here, mechanical and thermal sensory functions of rats were tested by von Frey and Hargreaves tests, respectively. We found that all animals started to recover partial mechanical sensation after 6 weeks from surgery (Figure 6A). The foot withdrawal thresholds in the rats treated by DNNA were lower, but no significant difference was found in three different strategies. The mechanical sensory function gradually recovered to the level of the sham control in all injured rats over time. The thermal sensation of rats treated by DNNA was found to recover to the level of the sham control 2 weeks post-surgery and kept a withdrawal latency time comparable to sham rats after that (Figure 6B). A statistical difference was observed between DNNA and fibrin glue groups at weeks 2 and 4, indicating that DNNA improved early thermal function recovery. Besides, faster thermal sensation recovery than mechanical recovery was noticed in all groups. The mechanisms behind are still not clearly understood.[44]

A rat-walking apparatus system was used to evaluate the recovery of locomotor functions by comparing the experimental foot (left hind in the system, LH) with the contralateral healthy foot (right hind in the system, RH) at week 10.[45, 46] The footprint intensity and foot pressure of transected nerve rats were significantly lower than those of sham group, and no statistical difference was noticed among nerve anastomosis groups for the foot pressure (Figure 6C). Rat body wobble was reflected by stance trace (Figure 6D). Perpendicular anterior extreme position (AEP) and posterior extreme position (PEP) recorded the foot position relative to the body center of paw touchdown and stance end, respectively.[47] Rats treated by DNNA illustrated comparable perpendicular AEP and PEP values with those of the sham, while they showed obvious body wobble, with AEP and PEP far from the body axis in the suture and fibrin glue groups (Figure 6E). Unequally distributed gait patterns with shorter stance phases (white squares) and extended swing durations (gray squares) were observed in all transected nerve animals (Figure 6F). This indicated hesitations of paw touchdown after nerve transection injury. However, a significantly longer stance duration was shown in DNNA repaired rats, suggesting better lower limb motor function recovery. Differences in the swing duration among the groups were statistically insignificant (Figure 6F).

2.7 DNNA decreases intraneural inflammation and fibrosis, and enhances nerve reconnection and remyelination

In section 2.5, we have demonstrated accelerated myelin and axon debris clearance in DNNA treated rats 10 days after surgery, which may be beneficial for long-term nerve regeneration. To further determine and verify the long-stage efficacy of DNNA treatments, nerves in different groups were harvested 10 weeks postoperatively. Here, the reconnection and remyelination of nerves were evaluated systematically.

According to nerve photographs, nerves were uniform in diameter with complete hydrogel degradation and without evidence of injury in the DNNA group, while suture and fibrin treated nerves showed bulges at the injury sites (Figure 7A). To further evaluate the structure continuity and connective tissue deposition of the treated nerves, we performed Masson’s Trichrome and H&E staining (Figure 7B and Figure S8A). Dense scar tissue surrounding the nerve trunk was distinguishable as bands of blue-stained collagen in the suture and fibrin groups, while there was much less collagen observed in the DNNA group (Figure 7B and 7C). Scar deposition also led to nerve thickening in the suture and fibrin repaired groups, which were twice larger in diameter compared to DNNA (Figure S8B). In addition, the fibrosis in the suture and fibrin groups was more severe compared with that at 10 days postoperatively, indicating persistent immune reactions and collagen depositions. As for the nerve continuity, fibrosis and foreign body reactions led to granuloma formation, structure disturbance, and nerve fiber misdirection in the suture coapted nerves (Figure 7B). Fibrin treated nerves showed intermittent nerve fiber distribution and poor reconnections with numerous connective tissues at the injury site. In contrast, directed nerve fiber regrowth and reconnection were demonstrated in the DNNA group, which was consistent with better sensory and motor function recovery described previously.

Myofibroblasts and macrophages are two important cells responsible for the excessive synthesis, deposition, and remodeling of collagens during fibrosis.[48] Immunofluorescence (IF) staining of alpha-smooth muscle actin (αSMA) showed a considerable increase of myofibroblast expression in the suture and fibrin groups, compared to the DNNA group (Figure 7D and 7E). We then performed CD68 IF staining to identify macrophages in sciatic nerves (Figure 7F). Nerves from sham rats showed rare CD68 positive cells, while suture and fibrin groups exhibited markedly increased macrophage numbers, especially for the fibrin group. DNNA alleviated long-term inflammation, compared to suture and fibrin, suggested by the decreased CD68 intensity and positive area (Figure 7G).

IF staining with TUBB3 and MBP was then performed to specifically assess axonal reconnection and myelination after nerve transection and repair (Figure 7H). Like previous histological staining results, the connection of TUBB3 positive axons was diverted and blocked by the granuloma in suture group, and misdirection and misalignment of nerve fibers were also noticed. Discontinuous and mussy axons were shown in fibrin group. In contrast, nerves treated by DNNA illustrated directed regrowth, and the density of the nerve fibers was significantly higher than that in the suture and fibrin groups (Figure 7I). Most importantly, more MBP positive myelin was observed in the DNNA group at the injury site, which was also confirmed by higher magnification images (Figure S8C).

We further studied the remyelination of regenerated nerves through toluidine blue staining and transmission electron microscopy (TEM) (Figure 8A). Nerve samples were collected from the distal ends and imaged in the cross-sectional directions. Toluidine blue images revealed much denser and larger neural fibers in the DNNA group than those in the suture and fibrin groups, indicating better regeneration and remyelination of DNNA treated nerves. However, all injured nerves had smaller nerve fibers and decreased myelin sheath thicknesses than the sham control. TEM examination also showed the presence of clusters of large, myelinated fibers in the DNNA group, in contrast to thin and sparse myelinated fibers in the suture and fibrin groups. Statistical analysis based on TEM images confirmed significantly increased sizes of myelinated axons (axon area in myelinated nerve fibers) and nerve fibers (including axon and myelin sheath) after treatment by DNNA, compared to suture and fibrin glues, though still smaller than native ones (Figure 8B and 8C). The G ratio of regenerated myelinated fibers, defined as the ratio of axonal area to nerve fiber area used for indicating optimal function and structure of neural myelination,[49] was also calculated. As shown in Figure 8D, the G ratio distribution trend of DNNA repaired nerves was comparable to that of the sham group, and the value of the G ratio gradually decreased following the order: fibrin glue group (0.35 ± 0.09) > suture group (0.30 ± 0.09) > DNNA group (0.28 ± 0.09) > sham nerve (0.27 ± 0. 07). In addition, the thickness of myelin sheaths from the DNNA group (1.15 ± 0.60 μm) was about 2 times higher than those from the suture (0.67 ± 0.23 μm) and fibrin glue (0.57 ± 0.19 μm) groups (Figure 8E).

In addition to fibrosis, macrophages also contribute to other pathogenic processes at the late stage of peripheral nerve repair. It was reported that persistent inflammatory responses with continuing macrophage presence impaired SC remyelination and suppressed nerve regeneration after injury.[50] Similar to results 10 days after surgery, the DNNA showed immune-regulatory behaviors in long term. It weakened intraneural inflammation and fibrosis, and enhanced nerve reconnection and remyelination, compared to suture and fibrin groups.

2.8 DNNA improves muscle structure and contraction force maintenance

Nerve related muscle structure and function maintenance is also a crucial aspect for nerve regeneration. We thus evaluated the weight, structure, and contraction force of the gastrocnemius muscles after treatment. Gastrocnemius muscles were harvested 10 weeks post-operation (Figure 9A), and the wet weight ratio (injured side/healthy side) was calculated. After injury and repair, the muscle weight was significantly decreased compared to sham group, but no statistical significance was noticed among different treatments (Figure 9B). Next, the morphology of the gastrocnemius muscles was studied by the H&E staining (Figure 9A). Of note, the DNNA group had significantly larger cross-sectional area of myofibers, compared to the suture and fibrin groups (Figure 9C). The maximum muscle contraction force was an important indication of muscle reinnervation and function after injury. The DNNA group illustrated muscle contraction force close to the sham group, with low standard deviation, and was significantly higher than the fibrin group (Figure 9D).

Taken together, our current design strategy of incorporating dopamine-isothiocyanate modified HA and decellularized matrix provides an efficacious adhesive hydrogel. For the first time, we demonstrated that our nerve adhesive was superior, or at least comparable (in some aspects), to commercial fibrin glue and microsurgical suture for peripheral nerve transection treatment. It can also inspire the development of other tissue adhesive systems, like gastrointestinal defect sealing (Supplemental Video S3 and S4). In addition, promising applications of DNNA as the bioactive cargo delivery system could be expanded in the future.[51–53] The DNNA could effectively connect the injured nerve ends, and deliver cells and therapeutic agents at the same time to further enhance nerve regeneration. Adipose-derived stem cells (ADSCs) and SCs have been reported to enhance axonal growth and lead to improved nerve repair *in vivo*.[53, 54] Drug-assisted treatments with neurotrophic factors, including nerve growth factors (NGF) and glial derived neurotrophic factors (GDNF), have potentials in the treatment of peripheral nerve injuries.[55] They play key roles in proliferation of Schwann cells and the survival of sensory and motor neurons. Sustained delivery of other therapeutic agents like magnesium (Mg) ions or extracellular vesicles can also stimulate the nerve regeneration process and facilitate nerve recovery.[52, 56]

Although promising, our current study has several limitations. Even though we can clearly illustrate the differences of axon and myelin clearance among different groups 10 days after surgery, to better understand whether delayed macrophage infiltration or the microenvironment led to delayed Wallerian degeneration, earlier time points after surgery still need to be investigated in a future study. In addition, the role of infiltrated macrophages in transected peripheral nerve repair at a late stage should be further confirmed on the cellular and molecular levels, and more detailed mechanisms can be revealed to identify how the DPN in the DNNA regulates immune response. Additional electrophysiological tests, like nerve conduction studies and compound muscle action potential, might be considered in the future study to evaluate the repaired peripheral nerve and the targeted muscle.

3 Conclusion

To summarize, we described a bioactive, dual-crosslinked, and high-efficacy nerve adhesive for nerve transection treatment. Our nerve adhesive exhibited fast and adjustable gelation behaviors and robust adhesion strength feasible for clinical applications. When applied to rat transected sciatic nerves, our adhesive significantly decreased intraneural inflammation and fibrosis, enhanced aligned axon connection and remyelination, as well as muscle function, compared to clinical suture and commercial fibrin treatments. These results collectively suggest that our nerve adhesive is a promising alternative to suture for nerve transection treatment.

4 Materials and methods

4.1 Study design

This study is dedicated to developing a nerve adhesive with robust adhesion strength and a bioactive composition for effective nerve transection treatment. The DNNA incorporated with catechol groups and decellularized nerve matrices was prepared to promote nerve regeneration and functional recovery of transected sciatic nerves. It was thoroughly characterized in terms of gelation behavior and mechanism, rheology, morphology, and adhesion performance. The *in vitro* biocompatibility was further tested to illustrate improved axonal outgrowth rendered by the addition of DPN. A sciatic nerve anastomosis model in rats was chosen to rigorously examine and compare the *in vivo* efficacy of the DNNA with a standard suture treatment and commercial fibrin glue. Nerve regeneration and functional recovery was characterized by sensory and motor behavior analysis every 2 weeks until the end of week 10. The gastrocnemius muscle contractile force and structure were determined to directly evaluate muscle atrophy. The histology, including fibrosis, foreign body reactions, axon reconnection, and myelination of injured nerves from the early stage (day 10) and late stage (week 10) was also examined.

4.2 Synthesis and characterization of HA-Cat

HA-Cat was synthesized according to the method reported previously.[22] Briefly, 0.5 g of HA powder (300 kDa, Bloomage Biotechnology Corporation Limited) and 0.25 g of $NaIO_4$ (Alfa Aesar) were dissolved in 50 mL of phosphate buffered saline (PBS, pH=5) and stirred for 5 h at room temperature (avoid light). Afterwards, 0.5 mL of ethylene glycol (Sigma-Aldrich) were added and stirred for another 1 h to neutralize the $NaIO_4$. The mixed solution was then dialyzed against deionized (DI) water for 2 days and lyophilized to obtain the aldehyde-modified HA.

To get dopamine conjugated HA, 0.5 g of aldehyde-modified HA were dissolved in PBS (pH=5). 0.5 g of dopamine hydrochloride (Combi-Blocks) were then added and stirred for 10 h at room temperature. After dialysis against DI water and lyophilization, the ^{1}H NMR spectrum was recorded on a 500 MHz Bruker NMR system. The DS was determined by the ratio of the integral of catechol methylene protons from the conjugated dopamine (between 2.8 ppm, $-CH_2$) to the integral of the HA methyl proton peak (at 2.0 ppm, $-CH_3$) using the equation $DS = 3 \times A_{2.8}/(2 \times A_{2.0})$.

4.3 Synthesis and characterization of HA-TU-Cat

HA-ADH was first synthesized. Briefly, 0.5 g of HA was dissolved in 100 mL of DI water. 1.2 g of 1-ethyl-3-(3-dimethylaminopropyl) carbodiimide hydrochloride (EDC, Combi-blocks), 1 g of HOBt hydrate (Oakwood Chemical), and 17 g of adipic dihydrazide (Tokyo Chemical Industry) were added. The pH of mixed solution was then adjusted to 6 and stirred at room temperature for 24 h. After the reactions were finished, the solution was dialyzed against sodium chloride (NaCl, Fisher Chemical) for 3 days and DI water for another 3 days and then lyophilized. The ^{1}H NMR was examined to confirm its successful synthesis.

Dopamine-isothiocyanate was then synthesized.[30, 60] Briefly, 6 g of dopamine hydrochloride were dissolved in 80 mL of tetrahydrofuran (Fisher Chemical) with 5.8 mL of triethylamine (Sigma-Aldrich). 82 mL of methanol (Fisher Chemical) were slowly added to help dissolution under the ice-cold conditions and nitrogen atmosphere. After forming a clear, colorless solution, 10 mL of carbon disulfide (Sigma-Aldrich) was added dropwise. The solution was left stirring for 2 h at 5–10 °C for reaction. The mixture was then warmed to room temperature while stirring for a further 10 to 12 h. The reaction mixture was cooled again to 5 °C, and 10 mL of 30 % hydrogen peroxide (H_2O_2, Fisher Chemical) were slowly added and stirred for 10 min under nitrogen atmosphere. The mixture was then neutralized with 37 % hydrochloric acid (HCl, Fisher Chemical, 2 mL). The resulting mixture was filtered and concentrated under vacuum. Then 50 mL of DI water and 50 mL of ethyl acetate (Alfa Aesar) were added into the mixture, and the crude product was purified by a silica column chromatograph (300–400 mesh, Acros Organics) using a chloroform/ethyl acetate (3:1, v/v) mixture. The final product was obtained as a white powder, and the ^{1}H NMR was recorded.

HA-TU-Cat was then obtained by dissolving 0.5 g of HA-ADH in 50 mL of DI water and reacting it with 0.3 g of dopamine-isothiocyanate powder in 50 mL of dimethyl sulfoxide (DMSO) for 3 days at room temperature (Figure 1A). The mixture was purified by dialysis against NaCl solution for 3 days and DI water for another 3 days. ^{1}H NMR was conducted, and the degree of substitution was calculated by the ratio of the integral of aromatic protons from the conjugated catechol group (between 6.5~7.0 ppm, $-C_6H_3$) to the integral of the HA methyl proton peak (at 2.0 ppm, $-CH_3$).

4.4 Decellularization of porcine peripheral nerves

Fresh porcine sciatic nerves (freshly isolated from five domestic pigs) were obtained from Tissue Source, LLC. Before decellularization, the fat tissues around the nerves were cleaned and removed. Then, the nerves were subjected to a combined chemical and enzymatic decellularization process.[61] Briefly, fresh nerves were stirred in 50 mM Tris buffer (pH=8) overnight and then in 1% Triton-X 100 in 50 mM Tris buffer solution at 4 °C for 24 h. The enzymatic treatment with 40 units/mL DNase (04536282001, Roche), 20 mg/L RNase (R4875, Sigma-Aldrich), and 0.01% Trypsin (Sigma-Aldrich) in Hank's Balanced Salt Solution (HBSS) was performed for 4 h at 37 °C. Then the nerves were stirred overnight in 1% Triton-X 100 in 50 mM Tris buffer at 4 °C. After lyophilization, the decellularized nerves were sterilized in 70% ethanol for 2 h and rinsed thoroughly with PBS. They were then cut into small pieces and digested in 1 mg/mL pepsin (Sigma-Aldrich) in 0.01 N HCl solution (with 20 mg/mL decellularized nerve). After constant agitation for 72 h at room temperature, the pH of the solution was adjusted to 7.5 by adding 1 N sodium hydroxide (NaOH, Fisher Chemical), and the salt concentration was adjusted by adding 10× PBS (1/10 of the final volume). This pre-gel solution was stored at −20 °C until use.

Histological sectioning and H&E staining were performed to verify the decellularization results. Native nerves and decellularized nerves were fixed in 10% formalin buffer for 4 h. After washing with PBS thrice, they were embedded in paraffin, sectioned, and stained by H&E. To determine the DNA, collagen, and GAG contents, native and decellularized nerve tissues were digested in 0.3 mg/mL papain solution (Sigma-Aldrich). The residual amount of DNA of NPNs and DPNs were quantitatively evaluated by a Quant-iT picoGreen kit (Invitrogen) following the manufacturer's procedures. The collagen contents were measured through a hydroxyproline assay, and the GAG contents were measured using a 1,9- dimethylmethylene blue (DMMB) assay, as described in our previous studies.[32, 62]

4.5 Preparation of HA-Cat and DNNA hydrogels

For HA-Cat adhesive hydrogel preparation, 2% HA-Cat was dissolved in PBS and mixed with MT at 37 °C (2500 U/mL, Sigma-Aldrich) or $NaIO_4$ at room temperature for 30 min (1:1 molar ratio of dopamine to $NaIO_4$). Note that the MT is a gentle and biocompatible oxidizing enzyme, compared to chemical oxidants like $NaIO_4$. However, to ensure successful gelation of the HA-Cat, $NaIO_4$ was also utilized here. 2% HA-TU-Cat was also dissolved in PBS and mixed with MT (500 U/mL). The solution was then incubated at 37 °C for 5 min to gelate.

To prepare the DNNA, 2% HA-TU-Cat in PBS was mixed with an equal volume of 20 mg/mL DPN pre-gel solution at 4 °C. MT (500 U/mL) was then added into the mixed solution and vortexed immediately. The whole solution was kept at 37 °C for 5 min to form physically and chemically double interacted hydrogel networks.

The influence of the DPN addition into HA-TU-Cat on its crosslinking mechanism was examined by UV-vis spectroscopy. The spectrum of the HA-TU-Cat and DNNA before and after oxidation was recorded over time in the wavelength range from 260 nm to 600 nm.

4.6 Rheological performance of nerve adhesives

The rheological performances of 1% DPN, 2% HA-Cat, 1% and 2% HA-TU-Cat, and DNNA were tested on a rheometer (HR-2, TA Instruments). The plate diameter was 20 mm, and the gap was 0.6 mm. The initial temperature of the plate was set as 4 °C to ensure liquidity of the pre-gel solutions. Then the plate temperature was rapidly increased to 37 °C at the rate of 100 °C /min, followed by a dynamic time sweep at the frequency of 1 Hz and 1% strain. The G' and G" of the hydrogels were recorded.

4.7 Morphology of nerve adhesives

For the morphological observation, 2% HA-Cat, 2% HA-TU-Cat, and DNNA were lyophilized and quenched in liquid nitrogen. Gold sputter coating was conducted, and they were observed by SEM (FEI Quanta 200) at 25 kV.

4.8 *In vitro* stability and swelling of nerve adhesives

For the stability evaluation, 50 µL of 2% HA-Cat, 2% HA-TU-Cat, and DNNA solutions were added into silicone molds with 6 mm diameters and formed hydrogels at 37 °C for 30 min. They were then incubated in PBS (pH=7.4) at 37 °C. At predetermined time points, the hydrogels were taken out of the PBS, rinsed with DI water, and lyophilized. The mass loss rate (%) was determined as: (original lyophilized hydrogel mass − lyophilized hydrogel mass at each time point)/ original lyophilized hydrogel mass × 100%.

As for the hydrogel swelling, lyophilized hydrogel samples were prepared and immersed in PBS (pH=7.4) at 37 °C. At specific time points, the mass of rehydrated hydrogels was measured. The swelling ratio (%) was calculated as: (rehydrated hydrogel mass at each time point − original lyophilized hydrogel mass)/ original lyophilized hydrogel mass × 100%.

4.9 Adhesion performances of nerve adhesives

The adhesion performances of HA-Cat, HA-TU-Cat, DNNA, and commercial fibrin glues (Tisseel) were evaluated by lap shear tests through porcine skins and tensile tests through rabbit nerves. The lap shear tests of nerve adhesives were conducted according to the ASTM F2255–05 standard.[63] Fresh porcine skins were bought from Nebraska Scientific and rinsed in PBS before removal of their fat layers. They were then cut into pieces of 20 mm in width and 40 mm in length. Then 0.2 mL of 2% HA-Cat/$NaIO_4$ (1:1 molar ratio), 2% HA-TU-Cat/MT (500 U/mL), 2% DNNA/MT (500 U/mL) solutions, or fibrin glue were applied onto the inner surface of one piece of porcine skin. It was covered by another porcine skin immediately, and the bonding area was 20 mm × 10 mm. All samples were kept at 37 °C for 30 min before measurements. Tests were performed on the Cellscale Univert tensile machine at a 6 mm/min take-up rate until failure. Force-displacement curves were recorded, and the adhesion strength was calculated as the failure force divided by the bonding area.

A tensile adhesion test determines the force required to pull adhesives off nerve surface. Rabbit sciatic nerves were collected from New Zealand White rabbits after euthanasia. The rabbits were euthanized subjects from another research protocol, which was approved by the Institutional Animal Care and Use Committee (IACUC) of the University of Nebraska Medical Center (UNMC). Rabbit nerves with lengths around 50–60 mm were cut into two halves. 20 μL of nerve adhesives prepared as formally mentioned were applied to one end of the cut nerve and connected with the other end immediately. All samples were kept at 37 °C for 30 min before tensile evaluations. Tests were conducted on the Cellscale Univert tensile machine at a 6 mm/min take-up rate until failure.

To further qualitatively demonstrate the utilization and feasibility of the DNNA, the isolated rabbit sciatic nerve was transected into three parts and reconnected with the DNNA at 37 °C for 5 min. In situ application on rabbits (after euthanasia) was conducted by connecting transected sciatic nerves for 5 min at room temperature. To evaluate adhesive performance of the DNNA under wet conditions, DNNA mixed with green food dye was first gelated on porcine skins and then twisted and immersed in PBS for 30 min. In addition, the DNNA was gelated on porcine skins and glass slides and was continuously flushed under water for 5 min.

4.10 *In vitro* SC and DRG culture in nerve adhesives

Rat SCs were isolated from fresh rat sciatic nerves, as previously reported.[32] 4×10^5 SCs/mL were suspended in 2% HA-TU-Cat/MT (500 U/mL) and DNNA/MT (500 U/mL) solution. Because $NaIO_4$ is cytotoxic, the 2% HA-Cat/$NaIO_4$ group was not included in the *in vitro* cell evaluations or *in vivo* experiments. 50 μL of SCs/adhesives mixed solutions were then added into silicone molds with 6 mm diameters and formed hydrogels at 37 °C for

30 min. Afterwards, SC culture medium, consisting of DMEM/low glucose medium (Cytiva HyClone™), 10% fetal bovine serum (FBS, Gibco), and 1% Pen/Strep (P/S, Gibco), was added and cultured for 7 days. A Live/Dead assay (Invitrogen) was applied to evaluate cell viability after 7 days of culture. The samples were imaged by a confocal laser scanning microscope (CLSM, LSM 710, Zeiss). The SC proliferation was determined at days 3 and 7 by a Cell Counting Kit 8 (CCK8, Abcam), following the manufacturer's protocol.

DRGs were dissected from 15-day-old mice (C57BL/6 background) from another research protocol, which was approved by the IACUC of UNMC. The dissected DRGs (from L4-L6 lumbar segments) were placed on 2% HA-TU-Cat/MT (500 U/mL) and 2% DNNA/MT (500 U/mL) hydrogels on glass slides (incubated at 37 °C for 30 min). After allowing DRG attachment on the adhesives at 37 °C for 1 h, DRG growth medium, consisting of DMEM/F12 medium (Cytiva HyClone™), 10% FBS, 1% P/S, and 10 ng/mL nerve growth factor (NGF, Peprotech), was added and cultured for 7 days. For IF staining of neurites from DRGs, the constructs were fixed in 4% paraformaldehyde (PFA) at 4 °C for 4 h and then rinsed with PBS. The samples were blocked by 1% bovine serum albumin (BSA) overnight at 4 °C. They were then incubated with primary antibodies to TUBB3 (1:400, rabbit, BioLegend) with 0.04% Triton X-100 in 1% BSA overnight at 4 °C. Alexa Fluor™ 568 goat anti-rabbit antibody (1:100 in 1% BSA) was then added and cultured for 2 h at room temperature. Finally, the cell nuclei were stained by DAPI (1:1000 in PBS) for 10 min. Imaging was performed with a 710 CLSM. The lengths of DRG neurites were quantified by the NeuronJ Plugin of Image J software, as reported in a previous study.[32]

4.11 *In vivo* peripheral nerve anastomosis

Animal experiments were approved by the IACUU of UNMC. A total of 40 female Sprague−Dawley rats (aged 9 weeks with weights ranging 170–250 g) were randomly divided into four groups: sham group (nerve was exposed without transection); suture group (nerve was transected and anastomosed with sutures); fibrin glue group (nerve was transected and anastomosed using commercial fibrin glue from Tisseel); DNNA group (nerve was transected and anastomosed with DNNA). Rats were anesthetized with isoflurane gas throughout the procedure. A skin incision was made parallel to the femur on the right side to expose the sciatic nerve. Afterwards, the sciatic nerve was transected with microsurgery scissors carefully under an operating microscope. For the suture group, end-to-end coaption of cut nerves was performed by two-stiches suturing (10–0 polyglycolic acid, Shapoint). For the fibrin glue and DNNA groups, 50 μL of the adhesives were applied onto the anastomosis site and cured for 5 min. Afterwards, the muscles and skins were sutured separately, and the rats received routine postoperative care and were kept in standard conditions. Random selected rats from suture, fibrin, and the DNNA groups were euthanized on day 10 for nerve collection. At the end of the experiment (week 10), rats from each group were anesthetized for muscle contraction testing. After animal euthanasia, the ipsilateral gastrocnemius muscles, sciatic nerves, L4/L5 DRGs, and spinal cords were harvested for further physiological and histological analysis.

4.12 Evaluation of sensory and motor function recoveries

The sensory and motor functions of the hindlimbs were evaluated based on behavior analyses, including von Frey, Hargreaves, and gait analysis tests, every two weeks post-surgery (weeks 2, 4, 6, 8, 10). To test the mechanical sensitivity, we confined the rats in boxes with a metal-mesh floor. After 30 min of habituation, we stimulated their experimental hind paws with von Frey filaments (Aesthesio) in incremental pressures (maximum of 50 g).[43, 64] Immediate foot lifting or licking was regarded as a withdrawal response. Five trials were conducted for each rat at intervals of 5 min, and the mechanical withdrawal threshold (g) was calculated as the mean of five consecutive trials. Thermal sensitivity was tested using a Hargreaves radiant heat apparatus (Ugo Basile Instrument), with an intensity of 45% and a cut-off time set as 30 s to avoid tissue damage. The latency of licking, withdraw, or shaking was recorded, and six trials for each rat were conducted with an interval of 10 min. To evaluate the rats’ locomotor functions, a homemade rat-walking apparatus based on a prototype of a MouseWalker system was utilized to analyze gait behaviors.[46] The apparatus was composed of a red backlit top panel, acrylic glass surrounded by green lights, a walking corridor above the glass, and a mirror at a 45-degree angle below the glass. Each rat received the training to walk from the entrance to the exit of the walking corridor before the test until there were no distractions or hesitation behaviors observed during the walking. During the test, rat walking was observed through the mirror and recorded by using a GoPro camera. The videos were uploaded into and run in the MouseWalker program in Matlab (Mathworks). The gait parameters for experimental hindlimbs of foot pressure; gait tracking information, including AEP and PEP; and stance and swing durations were quantified and compared to these of contralateral healthy hindlimbs.

4.13 Muscle characterization and contractile force

The rats were anesthetized with urethane (800 mg/kg ip) and α-chloralose (40 mg/kg ip) at week 10 to characterize the contractile force of gastrocnemius muscle. The gastrocnemius muscle was isolated, and its distal end was connected to a wide range force transducer (1030/D; AD Instruments, Colorado Springs). A bipolar hooked stimulating electrode was applied to the exposed sciatic nerve. To induce the tetanic contractile force of the gastrocnemius muscle, a constant-current stimulation was generated by a Grass S9 stimulator (Grass Instruments, West Warwick, RI, USA) at three times the motor threshold (defined as the minimum current required to produce a muscle twitch) with a pulse duration of 0.1ms at 50 Hz. After the measurement of muscle contraction force, the rats were sacrificed to harvest gastrocnemius muscles and measure their wet weights. Then the gastrocnemius muscles were fixed in 4% PFA overnight at 4 °C, embedded into paraffin, and sectioned (4 μm). H&E staining was conducted to evaluate the atrophy of myofibers in the gastrocnemius muscles by calculating their cross-sectional area by using ImageJ software. Images were taken from 3 randomly selected fields of each rat, and 3 rats in each group were analyzed.

4.14 Histological and morphological analyses

At day 10 post-surgery, sciatic nerves in the suture, fibrin, and DNNA groups were harvested and fixed in 4% PFA overnight at 4 °C. They were then embedded into paraffin, sectioned (4 μm), and subjected to H&E and Masson's Trichrome staining according to the standard protocols in the Tissue Science Facility at UNMC. For the IF staining, slides were deparaffinized and rehydrated, followed by antigen retrieval in heated citrate buffer for 20 min (citrate buffer solution, pH 6.0 at 100 °C).[65] Nonspecific antibody binding was blocked by 5% goat serum solution for 2 hours at room temperature, followed by overnight incubation at 4 °C with primary antibody in 0.04% Triton X-100 and 5% goat serum. Then corresponding secondary antibodies were added and incubated for 2 hours at room temperature. Samples were imaged by a 710 CLSM after nucleus staining with DAPI for 10 min. The primary antibodies used included TUBB3, MBP (1:400, rat, Millipore), and CD68 (1:100, mouse, AbboMax).

At week 10 post-surgery, sciatic nerves in the sham, suture, fibrin, and DNNA groups were harvested and fixed. H&E and Masson's Trichrome staining were conducted as mentioned before. For the IF staining, nerves were dehydrated in 30% sucrose overnight, embedded into optimal cutting temperature (OCT, Fisher HealthCare) compound, and cut into 10 μm sections for the staining of αSMA (1:200, mouse, Sigma-Aldrich), CD68, TUBB3, and MBP. For semiquantitative analysis of collagen, αSMA, CD68, and TUBB3 positive areas, randomly selected Masson's Trichrome and IF images from each group were split into three channels (red, green, and blue) in ImageJ software. By adjusting the threshold, target areas were measured and divided by the whole image area to calculate the target area ratios.

Nerve segments distal to the injury site were isolated and fixed with 2% glutaraldehyde and 2% paraformaldehyde in 0.1 M cacodylate buffer (pH 7.2). They were then transverse sectioned into 1 μm sections for toluidine blue staining and 100 nm sections for TEM using a Leica UC7 microtome. Toluidine blue images were observed with a brightfield microscope (DMi1, Leica). After a staining with 2% Uranyl Acetate and Reynolds Lead Citrate, sections for TEM were observed on a Tecnai G2 Spirit TWIN (Thermo Fisher Scientific) operating at 80 kV. Thirty images from 3 rats (ten images from each rat) from each group were randomly captured, and 300 nerve fibers were randomly selected for neural morphological analysis. The areas of axons and nerve fibers and the myelin thickness were measured using ImageJ. The area-based G ratio was further determined as the ratio of the axon area to the nerve fiber area.

4.15 Statistical analysis

All quantitative data were expressed as the mean ± standard deviation (SD). Statistical analysis was also performed. In experiments with two groups, Student's t-tests were used, while in experiments with more than two groups, one-way analysis of variance ANOVA was used with Tukey post-hoc tests for statistical analysis. Differences with $p<0.05$ were denoted as *, while $p<0.01$ was denoted as **, $p<0.001$ was denoted as ***, $p<0.0001$ was denoted as ****, and *ns* indicated not significant.

Supplementary Material

Refer to Web version on PubMed Central for supplementary material.

Acknowledgement

Funding: This work has been supported by University of Nebraska Collaboration Initiative Grant and NIH (R21AR078439) (B.D.).

Reference:

[1]. Menorca RM, Fussell TS, Elfar JC, Hand clinics 2013, 29, 317. [PubMed: 23895713]

[2]. Raza C, Riaz HA, Anjum R, Life sciences 2020, 243, 117308; [PubMed: 31954163] Hall S, The Journal of bone and joint surgery. British volume 2005, 87, 1309. [PubMed: 16189300]

[3]. Lundborg G, The Journal of hand surgery 2000, 25, 391; [PubMed: 10811744] Lee SK, Wolfe SW, JAAOS-Journal of the American Academy of Orthopaedic Surgeons 2000, 8, 243.

[4]. IJkema-Paassen J, Jansen K, Gramsbergen A, Meek M, Biomaterials 2004, 25, 1583. [PubMed: 14697860]

[5]. Isaacs J, Klumb I, McDaniel C, Journal of brachial plexus and peripheral nerve injury 2009, 4, e98;Lenoble E, Sokolow C, Ebelin M, Rigot J, Dabos N, Lemerle J, Vilain R, Annales de chirurgie de la main: organe officiel des societes de chirurgie de la main 1989, 8, 347; [PubMed: 2688574] Suri A, Mehta V, Sarkar C, Neurology India 2002, 50, 23. [PubMed: 11960146]

[6]. Wang ML, Rivlin M, Graham JG, Beredjiklian PK, Connective tissue research 2019, 60, 3. [PubMed: 30187777]

[7]. Sameš M, Blahoš J, Rokyta R, Beneš V, Physiol Res 1997, 46, 303. [PubMed: 9728497]

[8]. Millesi H, presented at Annales de Chirurgie de la Main 1984;Amoozgar Z, Rickett T, Park J, Tuchek C, Shi R, Yeo Y, Acta biomaterialia 2012, 8, 1849. [PubMed: 22310507]

[9]. Sameem M, Wood TJ, Bain JR, Plastic and Reconstructive Surgery 2011, 127, 2381; [PubMed: 21311390] Martins RS, Siqueira MG, Da Silva CF, Plese JP, Surgical neurology 2005, 64, S10;Egloff D, Narakas A, Annales de Chirurgie de la Main: Organe Officiel des Societes de Chirurgie de la Main 1983, 2, 101. [PubMed: 9336631]

[10]. Grinsell D, Keating C, BioMed research international 2014, 2014.

[11]. Temple C, Ross D, Dunning C, Johnson J, Journal of reconstructive microsurgery 2004, 20, 645. [PubMed: 15630661]

[12]. Tse R, Ko JH, Hand Clinics 2012, 28, 529. [PubMed: 23101603]

[13]. Yuk H, Varela CE, Nabzdyk CS, Mao X, Padera RF, Roche ET, Zhao X, Nature 2019, 575, 169; [PubMed: 31666696] Preul MC, Bichard WD, Muench TR, Spetzler RF, Neurosurgery 2003, 53, 1189; [PubMed: 14580287] Bu Y, Zhang L, Sun G, Sun F, Liu J, Yang F, Tang P, Wu D, Advanced Materials 2019, 31, 1901580.

[14]. Bouten PJ, Zonjee M, Bender J, Yauw ST, van Goor H, van Hest JC, Hoogenboom R, Progress in Polymer Science 2014, 39, 1375;Korde JM, Kandasubramanian B, Biomaterials Science 2018, 6, 1691. [PubMed: 29786707]

[15]. Wang D-A, Varghese S, Sharma B, Strehin I, Fermanian S, Gorham J, Fairbrother DH, Cascio B, Elisseeff JH, Nature Materials 2007, 6, 385; [PubMed: 17435762] Artzi N, Shazly T, Baker AB, Bon A, Edelman ER, Advanced materials 2009, 21, 3399. [PubMed: 20882504]

[16]. Sedó J, Saiz-Poseu J, Busqué F, Ruiz-Molina D, Advanced Materials 2013, 25, 653. [PubMed: 23180685]

[17]. Mädler S, Bich C, Touboul D, Zenobi R, Journal of mass spectrometry 2009, 44, 694. [PubMed: 19132714]

[18]. Taboada GM, Yang K, Pereira MJN, Liu SS, Hu Y, Karp JM, Artzi N, Lee Y, Nature Reviews Materials 2020, 5, 310.

[19]. Xu J, Liu Y, Hsu S.-h., Molecules 2019, 24, 3005. [PubMed: 31430954]

[20]. Guo Q, Chen J, Wang J, Zeng H, Yu J, Nanoscale 2020, 12, 1307; [PubMed: 31907498] Ahn BK, Das S, Linstadt R, Kaufman Y, Martinez-Rodriguez NR, Mirshafian R, Kesselman E, Talmon Y, Lipshutz BH, Israelachvili JN, Nature communications 2015, 6, 1;Zhou Y, Zhao J, Sun X, Li S, Hou X, Yuan X, Yuan X, Biomacromolecules 2016, 17, 622. [PubMed: 26779667]

[21]. Han L, Liu K, Wang M, Wang K, Fang L, Chen H, Zhou J, Lu X, Advanced Functional Materials 2018, 28, 1704195.

[22]. Zhou D, Li S, Pei M, Yang H, Gu S, Tao Y, Ye D, Zhou Y, Xu W, Xiao P, ACS applied materials & interfaces 2020, 12, 18225. [PubMed: 32227982]

[23]. Li A, Mu Y, Jiang W, Wan X, Chemical Communications 2015, 51, 9117; [PubMed: 25940100] Gan D, Xing W, Jiang L, Fang J, Zhao C, Ren F, Fang L, Wang K, Lu X, Nature communications 2019, 10, 1;Xie C, Wang X, He H, Ding Y, Lu X, Advanced Functional Materials 2020, 30, 1909954.

[24]. Lee HA, Park E, Lee H, Advanced Materials 2020, 32, 1907505;Thi TTH, Lee Y, Le Thi P, Park KD, Journal of Industrial and Engineering Chemistry 2019, 78, 34.

[25]. Zhang W, Wang R, Sun Z, Zhu X, Zhao Q, Zhang T, Cholewinski A, Yang FK, Zhao B, Pinnaratip R, Chemical Society Reviews 2020, 49, 433; [PubMed: 31939475] Paez JI, Ustahüseyin O, Serrano C, Ton X-A, Shafiq Z, Auernhammer G. n. K., d'Ischia M, del Campo A, Biomacromolecules 2015, 16, 3811. [PubMed: 26583428]

[26]. O'brien P, Chemico-biological interactions 1991, 80, 1. [PubMed: 1913977]

[27]. Bolton JL, Dunlap T, Chemical research in toxicology 2017, 30, 13; [PubMed: 27617882] Monks TJ, Hanzlik RP, Cohen GM, Ross D, Graham DG, Toxicology and applied pharmacology 1992, 112, 2. [PubMed: 1733045]

[28]. Asher R, Perides G, Vanderhaeghen JJ, Bignami A, Journal of neuroscience research 1991, 28, 410; [PubMed: 1713274] Tona A, Perides G, Rahemtulla F, Dahl D, Journal of Histochemistry & Cytochemistry 1993, 41, 593. [PubMed: 8450198]

[29]. Xu X, Xia X, Zhang K, Rai A, Li Z, Zhao P, Wei K, Zou L, Yang B, Wong W-K, Science Translational Medicine 2020, 12, eaba8014. [PubMed: 32848095]

[30]. Xu YJ, Wei K, Zhao P, Feng Q, Choi CKK, Bian L, Biomaterials science 2016, 4, 1726. [PubMed: 27722561]

[31]. Ikeda H, Ishikawa J, Hanamoto A, Shinose M, Kikuchi H, Shiba T, Sakaki Y, Hattori M, Ōmura S, Nature Biotechnology 2003, 21, 526;Suri S, Schmidt CE, Tissue Engineering Part A 2010, 16, 1703. [PubMed: 20136524]

[32]. Xue W, Kong Y, Abu R, Roy P, Huh S-H, Kuss M, Kumar V, Duan B, ACS Applied Materials & Interfaces 2022, 14, 8693. [PubMed: 35148064]

[33]. Crapo PM, Medberry CJ, Reing JE, Tottey S, van der Merwe Y, Jones KE, Badylak SF, Biomaterials 2012, 33, 3539. [PubMed: 22341938]

[34]. Jonker AM, Borrmann A, van Eck ER, van Delft FL, Löwik DW, van Hest JC, Advanced Materials 2015, 27, 1235. [PubMed: 25535032]

[35]. Schiessl WC, Summa NK, Weber CF, Gubo S, Dücker-Benfer C, Puchta R, van Eikema Hommes NJ, van Eldik R, Zeitschrift für anorganische und allgemeine Chemie 2005, 631, 2812.

[36]. Nam S, Mooney D, Chemical Reviews 2021.

[37]. Lee JI, Gurjar AA, Talukder M, Rodenhouse A, Manto K, O'Brien M, Govindappa PK, Elfar JC, Scientific reports 2020, 10, 1. [PubMed: 31913322]

[38]. Cerqueira SR, Lee Y-S, Cornelison RC, Mertz MW, Wachs RA, Schmidt CE, Bunge MB, Biomaterials 2018, 177, 176. [PubMed: 29929081]

[39]. Sun J-H, Li G, Wu T-T, Lin Z-J, Zou J-L, Huang L-J, Xu H-Y, Wang J-H, Ma Y-H, Zeng Y-S, Biomaterials 2020, 258, 120289. [PubMed: 32814215]

[40]. George R, Griffin JW, Journal of neurocytology 1994, 23, 657. [PubMed: 7861182]

[41]. Barnes CA, Brison J, Michel R, Brown BN, Castner DG, Badylak SF, Ratner BD, Biomaterials 2011, 32, 137. [PubMed: 21055805]

[42]. Coustry F, Gillery P, Maquart F-X, Borel J-P, FEBS letters 1990, 262, 339. [PubMed: 2335216]

[43]. Wang S, Zhu C, Zhang B, Hu J, Xu J, Xue C, Bao S, Gu X, Ding F, Yang Y, Biomaterials 2022, 280, 121251. [PubMed: 34810037]

[44]. Gorodetskaya N, Grossmann L, Constantin C, Jänig W, Journal of neurophysiology 2009, 102, 3129; [PubMed: 19741109] Jankowski MP, Lawson JJ, McIlwrath SL, Rau KK, Anderson CE, Albers KM, Koerber HR, Journal of Neuroscience 2009, 29, 1636. [PubMed: 19211871]

[45]. Croen BJ, Carballo CB, Wada S, Zhang X, Patel S, Deng XH, Rodeo SA, Journal of Orthopaedic Research® 2021, 39, 2243. [PubMed: 33336819]

[46]. Mendes CS, Bartos I, Márka Z, Akay T, Márka S, Mann RS, BMC biology 2015, 13, 1. [PubMed: 25555396]

[47]. Mendes CS, Bartos I, Akay T, Márka S, Mann RS, elife 2013, 2, e00231. [PubMed: 23326642]

[48]. Wynn TA, Vannella KM, Immunity 2016, 44, 450. [PubMed: 26982353]

[49]. Chew SY, Mi R, Hoke A, Leong KW, Advanced functional materials 2007, 17, 1288. [PubMed: 18618021]

[50]. Büttner R, Schulz A, Reuter M, Akula AK, Mindos T, Carlstedt A, Riecken LB, Baader SL, Bauer R, Morrison H, Aging cell 2018, 17, e12833. [PubMed: 30168637]

[51]. Warren D, Tomaskovic-Crook E, Wallace GG, Crook JM, APL bioengineering 2021, 5, 020901. [PubMed: 33834152]

[52]. Yao Z, Yuan W, Xu J, Tong W, Mi J, Ho PC, Chow DHK, Li Y, Yao H, Li X, Advanced Science 2022, 2202102; [PubMed: 35652188] Zhang J, Chen Y, Huang Y, Wu W, Deng X, Liu H, Li R, Tao J, Li X, Liu X, Advanced Science 2020, 7, 2002601. [PubMed: 33304766]

[53]. Yuan X, Yuan W, Ding L, Shi M, Luo L, Wan Y, Oh J, Zhou Y, Bian L, Deng DY, Biomaterials 2021, 279, 121190. [PubMed: 34736145]

[54]. Jahromi HK, Farzin A, Hasanzadeh E, Barough SE, Mahmoodi N, Najafabadi MRH, Farahani MS, Mansoori K, Shirian S, Ai J, Materials Science and Engineering: C 2020, 109, 110564; [PubMed: 32228906] Sun AX, Prest TA, Fowler JR, Brick RM, Gloss KM, Li X, DeHart M, Shen H, Yang G, Brown BN, Biomaterials 2019, 203, 86. [PubMed: 30857644]

[55]. Lackington WA, Kočí Z, Alekseeva T, Hibbitts AJ, Kneafsey SL, Chen G, O'Brien FJ, Journal of Controlled Release 2019, 304, 51; [PubMed: 31054993] Fadia NB, Bliley JM, DiBernardo GA, Crammond DJ, Schilling BK, Sivak WN, Spiess AM, Washington KM, Waldner M, Liao H-T, Science Translational Medicine 2020, 12, eaav7753. [PubMed: 31969488]

[56]. Yu M, Gu G, Cong M, Du M, Wang W, Shen M, Zhang Q, Shi H, Gu X, Ding F, Acta Biomaterialia 2021, 134, 190. [PubMed: 34289422]

[57]. Zhou H, Liang C, Wei Z, Bai Y, Bhaduri SB, Webster TJ, Bian L, Yang L, Materials Today 2019, 28, 81;Yuan W, Li Z, Xie X, Zhang Z-Y, Bian L, Bioactive Materials 2020, 5, 819. [PubMed: 32637746]

[58]. Pascual G, Sotomayor S, Rodriguez M, Pérez-Köhler B, Kühnhardt A, Fernandez-Gutierrez M, San Román J, Bellón JM, PloS one 2016, 11, e0157920. [PubMed: 27322731]

[59]. Lauto A, Mawad D, Foster LJR, Journal of Chemical Technology & Biotechnology: International Research in Process, Environmental & Clean Technology 2008, 83, 464.

[60]. Medintz IL, Stewart MH, Trammell SA, Susumu K, Delehanty JB, Mei BC, Melinger JS, Blanco-Canosa JB, Dawson PE, Mattoussi H, Nature materials 2010, 9, 676; [PubMed: 20651808] Ji X, Palui G, Avellini T, Na HB, Yi C, Knappenberger KL Jr, Mattoussi H, Journal of the American Chemical Society 2012, 134, 6006. [PubMed: 22394283]

[61]. Philips C, Campos F, Roosens A, del Carmen Sanchez-Quevedo M, Declercq H, Carriel V, Annals of biomedical engineering 2018, 46, 1921. [PubMed: 29987538]

[62]. Duan B, Kapetanovic E, Hockaday LA, Butcher JT, Acta biomaterialia 2014, 10, 1836. [PubMed: 24334142]

[63]. A. S. f. Testing, Materials, Standard Test Method for Strength Properties of Tissue Adhesives in Lap-Shear by Tension Loading, ASTM International, 2005.

[64]. Kong Y, Shi W, Zhang D, Jiang X, Kuss M, Liu B, Li Y, Duan B, Applied Materials Today 2021, 24, 101090.

[65]. Janjic JM, Vasudeva K, Saleem M, Stevens A, Liu L, Patel S, Pollock JA, Journal of neuroimmunology 2018, 318, 72. [PubMed: 29519721]

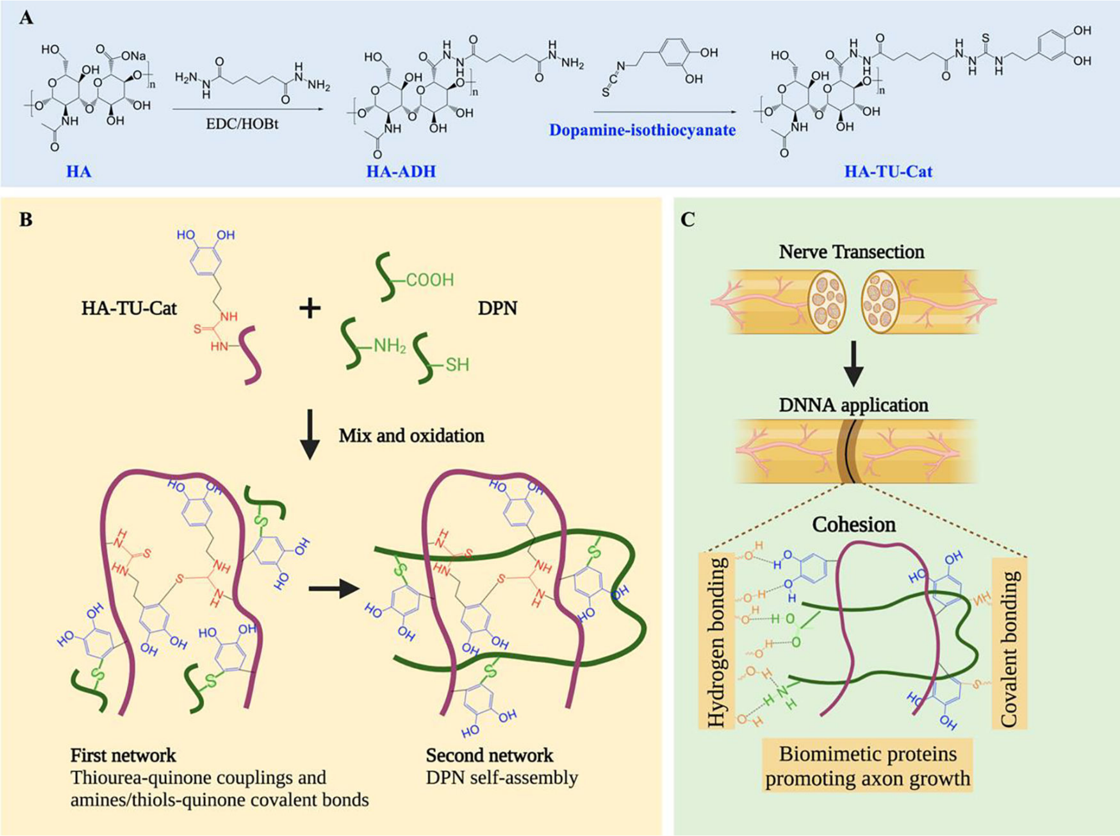

Figure 1.

Schematic illustration of DNNA fabrication. (A) Schematic of the synthesis process of HA-TU-Cat. (B) Schematic illustrating the formation of two interacting networks in DNNA composed of HA-TU-Cat and DPN. (C) Adhesion mechanism of DNNA via hydrogen bonding of neutrophils from DPN and covalent bonding of catechol from HA-TU-Cat to nerve tissues. DPN provides biomimetic proteins to promote axonal growth.

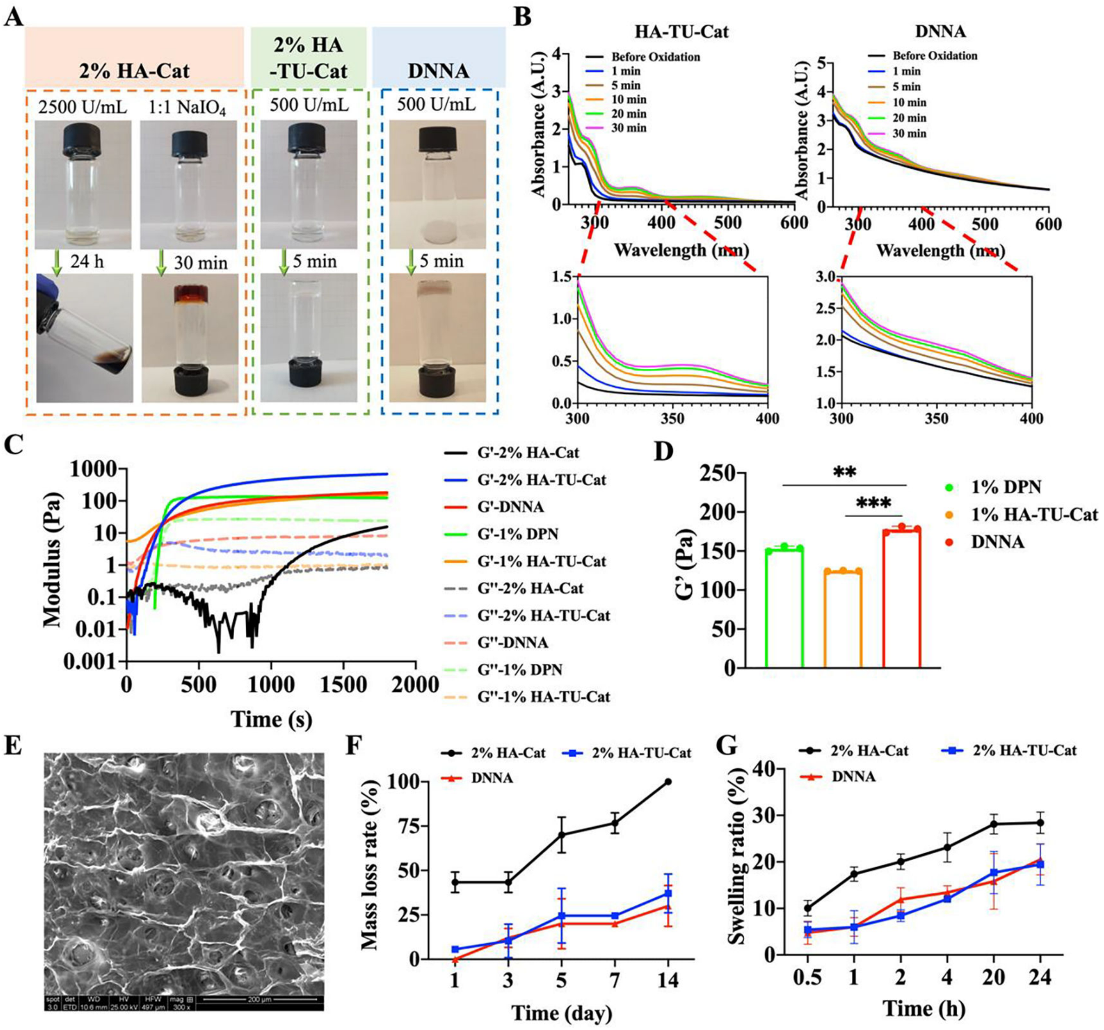

Figure 2.

Physical and chemical characterizations of DNNA. (A) Photographs showing gelation of 2% HA-Cat, 2% HA-TU-Cat, and DNNA. (B) UV-Vis spectra of HA-TU-Cat and DNNA before and after oxidation over time. Insets: UV-Vis spectra of HA-TU-Cat and DNNA in the wavelength range of 300–400 nm. (C) Storage (G') and loss (G") moduli of HA-Cat, HA-TU-Cat, DPN, and DNNA recorded in a time sweep. (D) G' of 1% DPN, 1% HA-TU-Cat, and DNNA (n=3). (E) SEM of DNNA hydrogels. (F) Mass loss rate (%), and (G) swelling ratio (%) of 2% HA-Cat, 2% HA-TU-Cat, and DNNA in PBS at 37 °C (n=3–4). All quantitative data are expressed as the mean ± standard deviation. Asterisks indicate statistically significant comparisons, with $^{**}p < 0.01$ and $^{***}p < 0.001$, by Student's t-test or one-way ANOVA with Tukey's multiple comparisons tests.

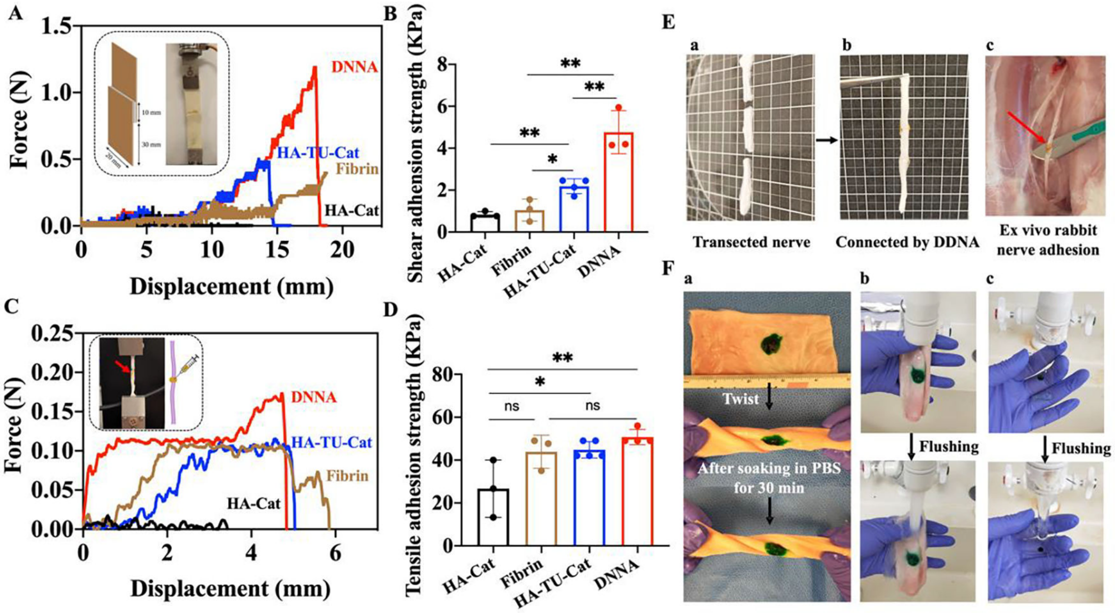

Figure 3.

Quantitative and qualitive determination of DNNA adhesion performances. (A) Force-displacement curves of HA-Cat, fibrin, HA-TU-Cat, and DNNA under lap shear measurement through fresh porcine skins. Inset: Illustration of the lap shear measurement. (B) Shear adhesion strength of HA-Cat, fibrin, HA-TU-Cat, and DNNA (n=3–4). (C) Force-displacement curves of HA-Cat, fibrin, HA-TU-Cat, and DNNA under tensile measurement through rabbit sciatic nerves. Inset: Illustration of the tensile measurement. (D) Tensile adhesion strength of HA-Cat, fibrin, HA-TU-Cat, and DNNA (n=3–5). (E) Qualitive adhesion evaluation of DNNA through rabbit sciatic nerves. Rabbit nerve was cut into three parts (a); The transected nerves were successfully connected by DNNA (b); In situ rabbit nerve adhesion (c). (F) Qualitive adhesion evaluation of DNNA under deformations and wet environments. DNNA (with green food dye) formed on porcine skin in situ was twisted and soaked in PBS for 30 min (a); DNNA formed on the porcine skin in situ was flushed continuously for 5 min (b); DNNA formed on the glass slide in situ was flushed continuously for 5 min (c). All quantitative data are expressed as the mean ± standard deviation. Asterisks indicate statistically significant comparisons, with $*p < 0.05$ and $**p < 0.01$, by Student’s t-test or one-way ANOVA with Tukey’s multiple comparisons tests.

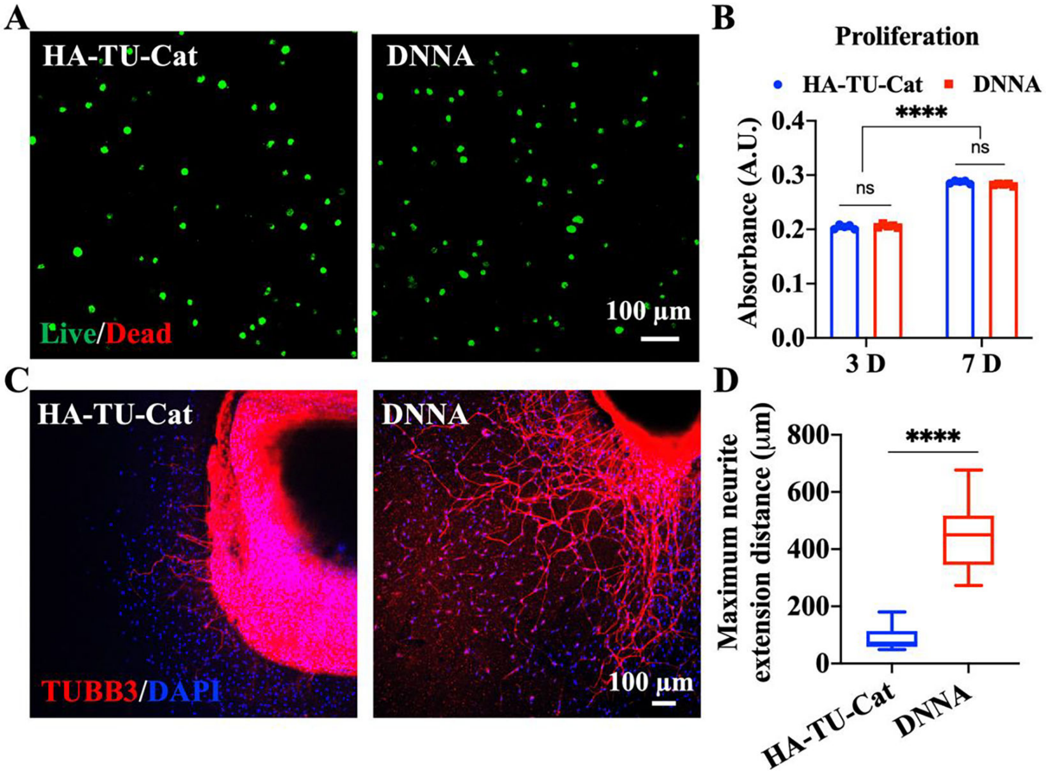

Figure 4.

In vitro biocompatibility of DNNA. (A) Livability of SCs encapsulated in HA-TU-Cat and DNNA hydrogels after 7 days. Red: dead cells; green: live cells. (B) Proliferation of SCs encapsulated in HA-TU-Cat and DNNA hydrogels tested by CCK8. (C) Axonal outgrowth from DRGs on HA-TU-Cat and DNNA hydrogels. Red: TUBB3 stained axon; blue: DAPI stained nucleus. (D) Maximum axonal extension distance from DRGs on HA-TU-Cat and DNNA hydrogels. 20–30 axons from 4 DRGs were included in each group. All quantitative data are expressed as the mean ± standard deviation. Asterisks indicate statistically significant comparisons, ****p<0.0001, by Student’s t-test.

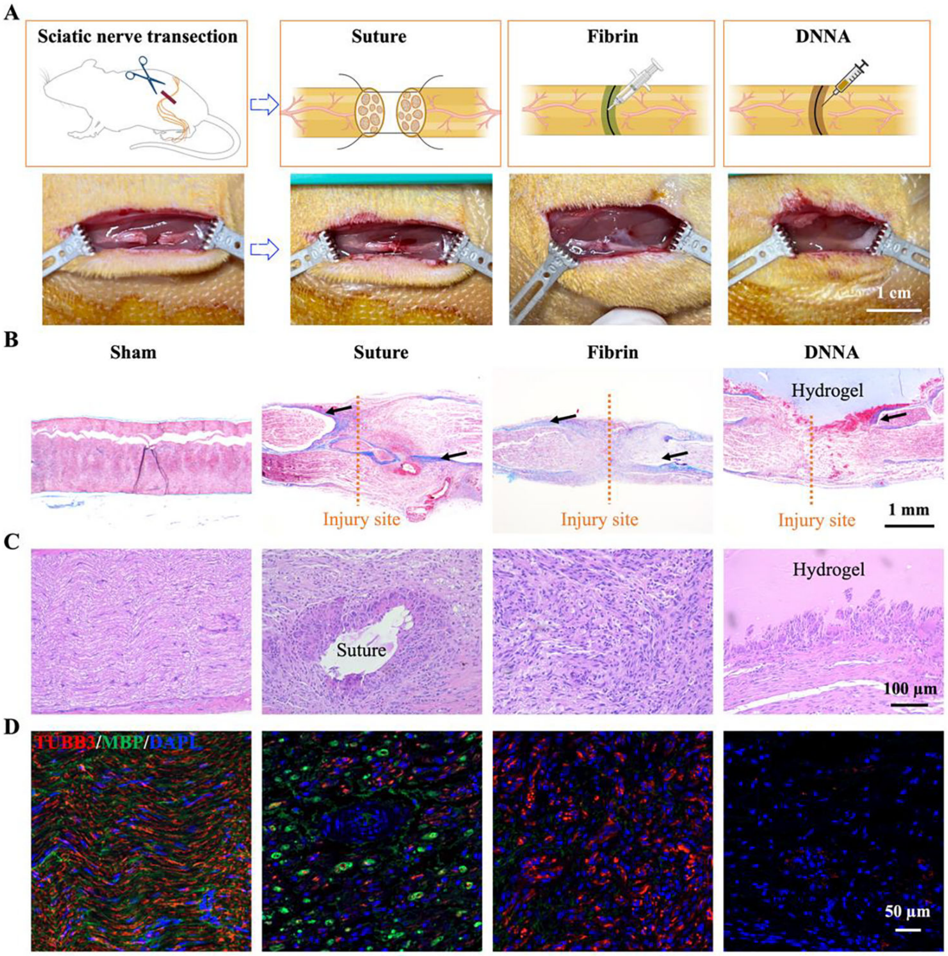

Figure 5.

In vivo peripheral nerve anastomosis in a rat model and nerve histological evaluation on day 10 postoperatively. (A) Schematic illustrating the transection and anastomosis of rat sciatic nerves through suture, fibrin glue, and DNNA. (B) Masson's Trichrome staining of sham nerve, suture, fibrin, and DNNA treated nerves 10 days postoperatively. (C) H&E staining of sham nerve, suture, fibrin, and DNNA treated nerves 10 days postoperatively. (D) Axon and myelin debris determination at the injury site 10 days postoperatively. Red: TUBB3 stained axon; green: MBP stained myelin sheath; blue: DAPI stained nucleus.

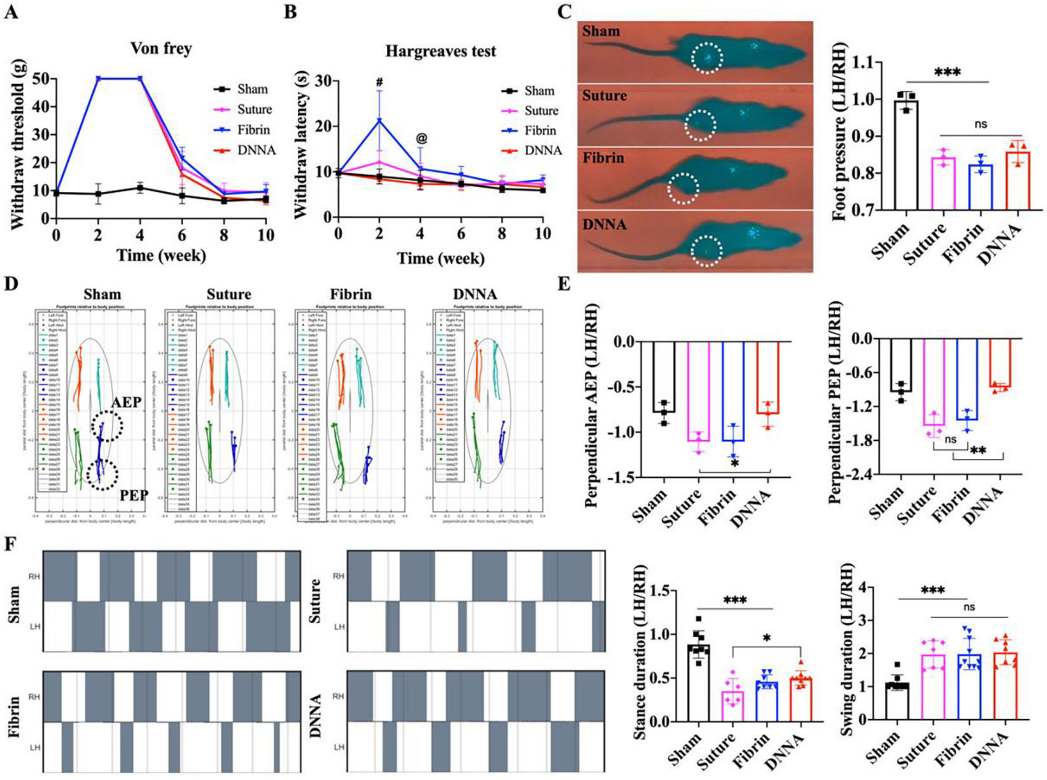

Figure 6.

Sensory and motor function recovery of rats with transected nerve injuries. (A) Mechanical sensory functions of rats tested by a von Frey test over time (n=6). (B) Thermal sensory functions of rats tested by a Hargreaves test over time (n=6). #: $p<0.001$ between DNNA and Fibrin; @: $p<0.05$ between DNNA and Fibrin. (C) Footprints were captured by a rat-walking apparatus, and the foot pressure ratio was calculated as LH/RH at 10 weeks after surgery (n=3). (D) Stance trace of rats at 10 weeks after operation. (E) Perpendicular AEP and PEP ratios (LH/RH) demonstrating body wobble (6–10 steps from 3 rats in each group). (F) Stance/swing durations of each group and their ratios of experimental foot to healthy foot (LH/RH, 6–10 steps from 3 rats in each group). All quantitative data are expressed as the mean ± standard deviation. Asterisks indicate statistically significant comparisons, with $*p < 0.05$, $**p < 0.01$, and $***p < 0.001$, by Student's t-test or one-way ANOVA with Tukey's multiple comparisons tests.

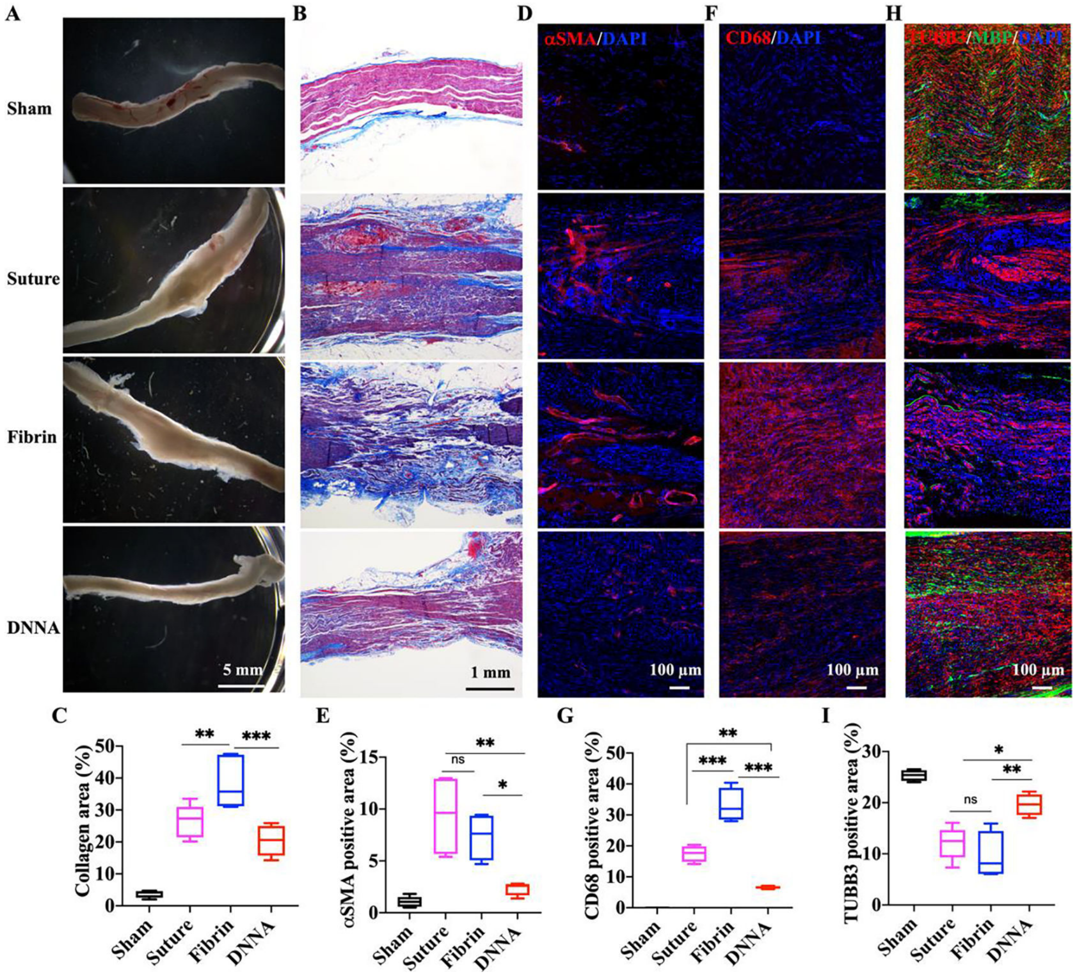

Figure 7.

Histological analysis of injured nerves 10 weeks after surgery. (A) Photograph of harvested nerves in the sham, suture, fibrin, and DNNA groups. (B) Masson's Trichrome staining of nerves in each group. (C) Semi-quantification of collagen areas in each group (n=4–6). (D) Myofibroblast determination by IF staining. Red: αSMA stained myofibroblasts, blue: DAPI stained nucleus. (E) Semi-quantification of αSMA positive areas in each group (n=4–6). (F) Macrophage determination by IF staining. Red: CD68 stained macrophages, blue: DAPI stained nucleus. (G) Semi-quantification of CD68 positive areas in each group (n=4–6). (H) Axon and myelin determination by IF staining. Red: TUBB3 stained axons, green: MBP stained myelin, blue: DAPI stained nucleus. (I) Semi-quantification of TUBB3 positive areas in each group (n=4–6). All quantitative data are expressed as the mean ± standard deviation. Asterisks indicate statistically significant comparisons, with *$p < 0.05$, **$p < 0.01$, and ***$p < 0.001$, by Student's t-test or one-way ANOVA with Tukey's multiple comparisons tests.

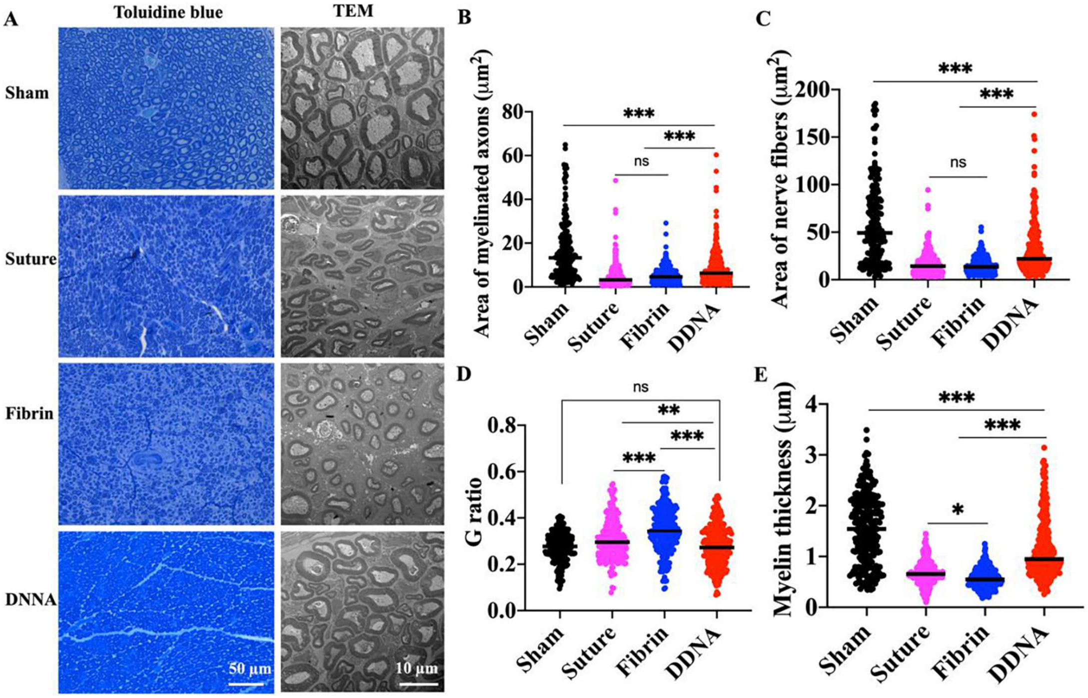

Figure 8.

Nerve remyelination at the distal segment after 10 weeks. (A) Nerve cross-sections stained with toluidine blue and TEM images at the distal site. (B-E) Quantitative data analysis by measuring the average area of single myelinated axons (B), the average area of single neural fibers (C), area-based G-ratio (D), and myelin thickness (E), in different groups according to TEM images. 300 axons from 3 rats in each group were included. All quantitative data are expressed as the mean ± standard deviation. Asterisks indicate statistically significant comparisons, with *$p < 0.05$, **$p < 0.01$, and ***$p < 0.001$, by Student's t-test or one-way ANOVA with Tukey's multiple comparisons tests.

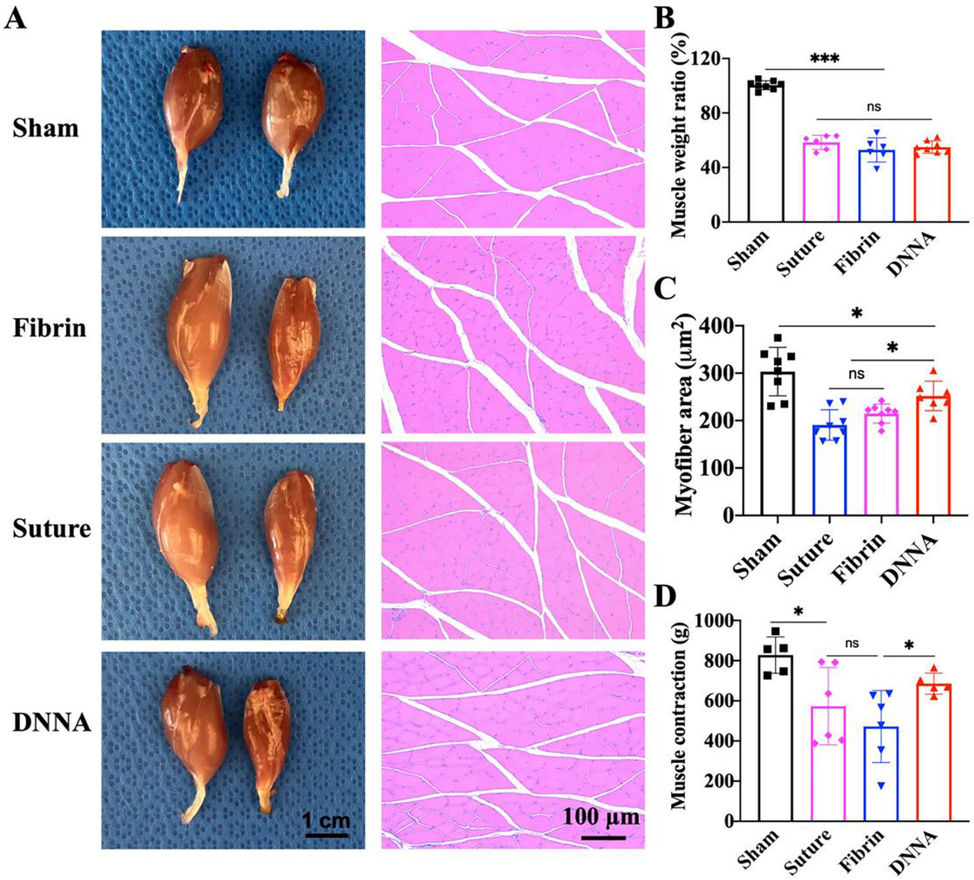

Figure 9.

Characterizations of gastrocnemius muscle function at week 10. (A) Photographs (left: contralateral; right: ipsilateral) and corresponding cross-sectional H&E staining of gastrocnemius muscles of each group. (B) Wet gastrocnemius muscle weight ratio (ipsilateral to contralateral, n=6–8). (C) Average size of single myofiber of gastrocnemius muscles (n=6–8). (D) Maximum muscle contraction force of the experimental leg (n=5–6). All quantitative data are expressed as the mean ± standard deviation. Asterisks indicate statistically significant comparisons, with $*p < 0.05$, $**p < 0.01$, and $***p < 0.001$, by Student’s t-test or one-way ANOVA with Tukey’s multiple comparisons tests.